MEASUREMENTS OF PION CHARGE EXCHANGE AND OTHER THINGS AT FERMILAB ENERGIES

Thesis by

Alan Voltz Barnes

In Partial Fulfillment of the Requirements

for the Degree of

Doctor of Philosophy

California Institute of Technology

Pasadena, California

1980

(submitted February 4, 1980)

ACKNOWLEDGMENT

There are no one person particle physics experiments. To make one of these experiments a success takes the concerted effort of many people. I would like to take this opportunity to thank those people who made this experiment a success. First I thank my collaboraters Orin Dahl, Bob Kenney and Morris Pripstien from Lawrence Berkeley Laboratory; and Joel Mellema, Alvin Tollestrup and, my advisor, Robert Walker from here at Caltech. Next are those who gave us the technical support. Fritz Bartlett gave us excellent software support. Dave Hermeyer gave us electronic support and helped in collecting the data. Finally I would like to thank the technical staff of Lawrence Berkeley Laboratory and that of our own shops without whom none of this would have been possible. Just as there are no one person experiments, there are no one person educations. I would like to thank those people who influenced me in my stay at Caltech. I thank C. Peck and G. Zweig for teaching a lot about how to think. I thank Ricardo and Clara Gomez for teaching me a lot about how to live. I thank Ted Barnes for teaching me a lot about how to get inspired. I also thank all my teachers and fellow students for the environment they provided. Finally, I would like to give special thanks and dedicate this thesis to Vaughn Davidson with whom and from whom I learned almost everything I know.

MEASUREMENTS OF PION CHARGE EXCHANGE AND OTHER THINGS AT FERMILAB ENERGIES

ABSTRACT

This paper presents the results of experiment 111 at Fermilab. The experiment was designed to measure the pion nucleon charge exchange reaction ($\pi^-p \rightarrow \pi^0 n$). The apparatus used allowed collection of data on many other reactions of the type $\pi^-+p \rightarrow$ (photons)+n. Data are presented here for the two body reactions with π^0, η, η' and $\delta(980)$ in the final state. Data on the π^0 and η have appeared elsewhere (reference 1-1).

CONTENTS

1. Introduction

Physics is the study of what things are and how they behave. It progresses through a series of steps. At the first step we describe the things and their behavior. At the second we search for regularities in our descriptions. At the third we attempt to find ideas which will allow us to understand these regularities. And finally we reformulate our initial descriptions in terms of these presumably more fundamental ideas. Thus we come back to the first step in our never ending path toward an understanding of what things are and how they behave.

Along this path are many turns and forks. Some represent good ways of thinking about things, but many lead us into confusion and away from reality. In our studies we must explore each turn and fork enough to determine whether it leads to reality or confusion. To this end we formulate ideas and test them against observations. In this way theory and experiment working together choose paths toward greater understanding of what things are and how they behave.

In our studies of the strong interaction we are at the threshold of confusion. Much as the regularities and peculiarities of atomic systems confused the physicists of

the first decade of this century; the spectra and reactions of the hadrons confuse us today. But, as the spectral studies of their day led them through their confusion; so, we hope, will studies of hadron properties and reactions lead us through ours.

Observations of the past thirty years show us many regularities. Regularities of the hadron masses, spins and other quantum numbers led Gell-Mann (reference 1-2) and Zweig (reference 1-3) to invent the quark model. This quark model, supplemented with a new kind of charge called color and with particles which couple to this charge called gluons (reference 1-4), is proving to be a very good way of describing many features of the hadrons and the strong interaction. However, many reactions show amazing regularities and simplicities which this theory, Quantum Chromodynamics (QCD), has not yet explained. Further study of these reactions should provide us with more information from which to extract insight into the difficulties causing the confusion we face.

One of the more striking features of hadron dynamics shows up in two body scattering reactions. If we look at these reactions as an exchange of some particle between the reactants as in figure 1-1, we notice that those reactions where the quantum numbers exchanged are the same as those of

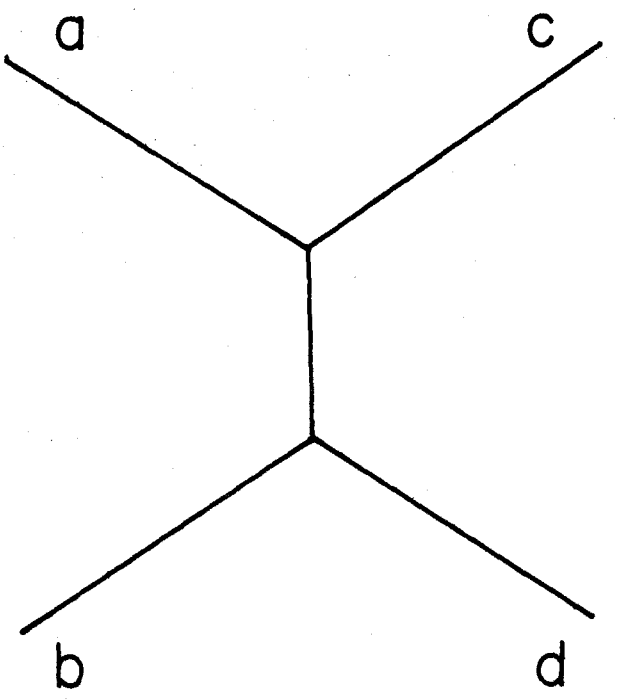

Exchange diagram for the reaction

$$a + b \rightarrow c + d$$

Definition of the Mandlestam variables in terms the four momenta of the reactants

$$s = (P_a + P_b)^2 = (P_c + P_d)^2$$

$$t = (P_a - P_c)^2 = (P_b - P_d)^2$$

$$u = (P_a - P_d)^2 = (P_b - P_c)^2$$

figure 1-1

a real particle have peaks in their differential cross sections at small scattering angles. A naive form of Regge's idea (reference 1-5) of extending the scattering amplitude into complex angular momentum space works suprisingly well. It relates the energy dependence of the small angle differential cross section to the masses and spins of the particles with the quantum numbers exchanged in the reaction. Barger and Cline give a nice presentation of this regularity in their book "Phenomenological Theories of High Energy Scattering" (reference 1-6).

From the Regge point of view the pion nucleon charge exchange reaction

$$\pi^- + p \rightarrow \pi^0 + n \qquad \text{(CEX)}$$

shows great simplicity. The quantum numbers exchanged in the reaction are those of the family of particles associated with the ρ meson trajectory. Although the exchange of other particle trajectories should occur, the Regge idea indicates these exchanges should become unimportant at high energies. For a simple Regge pole model the differential cross section should vary like

$$d\sigma/dt = \beta(t)\,\nu^{2\alpha(t)-2}$$

where t is the Mandlestam momentum transfer variable,

$\beta(t)$ is an arbitrary function of t,

$\alpha(t)$ is the ρ meson Regge trajectory,

is $(s-u)/s_0$

and s_0 is a scale energy chosen for convenience to be four energy units times the proton mass.

Although our primary motivation for studying this reaction is its simplicity from the Regge viewpoint, this is by no means its only interesting aspect. The reactions between pions and nucleons show a simplicity which we call the principle of isospin invariance. According to this principle the strong interaction conserves the total isospin and the reaction amplitude depends on the total isospin of the state but not on its projection.

Isospin was introduced as a formal way of expressing the idea that the neutron and proton are really just different states of the same particle. Composite systems of particles with isospin can be decomposed into isospin states using the same algebraic formalism used for decomposition of angular momentum. Thus we can combine an isospin 1 pion and an isospin 1/2 nucleon and get the isospin 1/2 and isospin

3/2 parts. Since the principle states the amplitude depends only on the total isospin, we can use it to relate amplitudes for otherwise different processes. In our example we relate the amplitudes for elastic scattering of charged pions to the charge exchange amplitude as follows:

$$A(CEX)=[A(\pi^+ p \rightarrow \pi^+ p)-A(\pi^- p \rightarrow \pi^- p)]/\ 2$$

There are three especially interesting features of the scattering amplitude in the extreme forward direction: there is only one helicity amplitude; the optical theorem relates the total cross sections for the charged pions to the imaginary parts of their elastic amplitudes; and, the Coulomb scattering amplitude is large enough to be used to measure the phases of the elastic amplitudes. These features combined with isospin invariance allow seven experimental measurements to be combined to determine the four numbers required to specify the two isospin amplitudes. Thus the detailed measurements of pion-nucleon elastic scattering, total cross sections, Coulomb interference and charge exchange scattering provide an interesting test of the isospin invariance of the strong interaction.

I now turn to a description of the final state which our experiment detected. The final state in pion-nucleon

charge exchange consists of a π^o and a neutron. We know that the differential cross section at lower energies is appreciable only when the π^o is produced in the forward direction. In fact we expect the final state neutron to have a very low energy and the π^o, which decays into two photons, to have almost all of the energy of the incident pion. To detect the π^o's we constructed a photon detector which was big enough to detect both the photons from most of the π^o's produced out to a momentum transfer, t, of -4 GeV^2. Since our data collection system made no distinction between events with two photons and those with many photons, we were also able to collect data on other reactions which have only a neutron and photons in the final state.

2. The Apparatus

The equipment used to perform these measurements consisted of a beam of projectile particles, a target and a detection system.

The beam was the M2 beam of the Meson Laboratory at the Fermilab. The particles were produced by focusing high energy protons from the synchrotron on a solid target where interactions occurred yielding particles of various types, charges, energies and angles. Particles of the desired charge and momentum were selected and focused with a system of magnets and collimators. The beam line was instrumented with scintillation counters to count the incident beam particles, a scintillation counter hodoscope to measure their trajectories and a threshold Cerenkov counter to separate the low mass pions, muons and electrons from the higher mass kaons and antiprotons.

The beam transport system was used to focus the particles onto a liquid hydrogen target where the interactions to be studied took place.

This target was surrounded by a detector system designed to allow the identification of neutral final state reactions. All the solid angle except the beam entrance was

covered by scintillation counters to reject interactions with charged reaction products. In the forward direction there was a photon detector to measure the positions and energies of the photons coming from the reaction. The solid angle not covered by the photon detector was largely covered by lead and plastic shower counters to detect other photons from the reaction.

2.1 The Hydrogen Target

Our target consisted of two cylindrical flasks of liquid hydrogen arranged in line with one another on the beam axis. The upstream flask was 15.8 inches long and 2 1/2 inches in diameter while the downstream flask was 8 inches long and 3 inches in diameter. They could be filled independently and were used in all four of their possible configurations during the collection of data for this experiment. The hydrogen density was monitored by a pressure gauge in the gas above the hydrogen liquid. A more detailed description of this target may be found in Randy Johnson's thesis (reference 2-1).

2.2 The Beam

This experiment was run in the M2 beam of the Meson laboratory of the Fermilab. During the running of the

experiment Fermilab was being upgraded from its design energy of 200 GeV to an energy of 400 GeV. As a result there was a continuing program of adding magnets and power supplies to the M2 beam line to enable it to make use of the higher energies available. While this upgrading allowed the experiment to be performed at higher energies, it also required continual retuning of the beam line and made precise energy calibration difficult. The final energy calibration came from the data and is described in detail in section 4.4.

Although the magnets and power supplies changed the idealization of these elements was unchanged. An optical idealization is shown in figure 2-1. The layout was such that the momentum dispersion at the first focus was about 1% per inch. The momentum acceptance was set by the width of the collimator C5 at the first focus and varied between 1% and 2% during the data collection. The beam intensity varied between 10^5 and 10^6 particles per one second accelerator pulse.

The beam was instrumented with two scintillation counter hodoscopes to measure incoming particle positions and angles, a threshold Cerenkov counter to tag particle types, a scintillation counter telescope to count the beam particles and a scintillation counter with a hole to veto

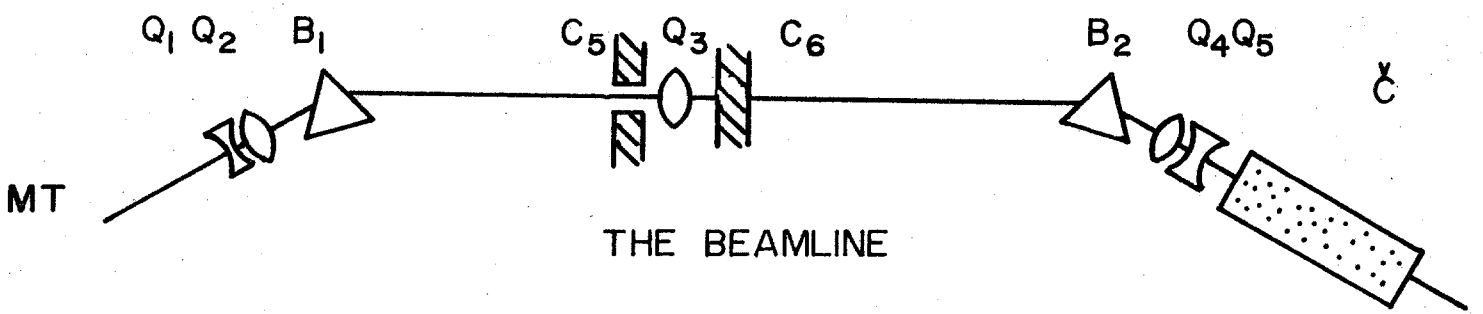

Element	Device	Function
MT	Production Target	Source of Secondary Particles
Q1	Quadrapole Magnet	Focusing
Q2	Quadrapole Magnet	Focusing
B1	Dipole Magnet	Bending
C5	Horizontal Collimator	Momentum Selection
Q3	Quadrapole Magnet	Intensity Enhancement
C6	Verticle Collimator	Intensity Control
B2	Dipole Magnet	Bending
Q4	Quadrapole Magnet	Focusing
Q5	Quadrapole Magnet	Focusing
C	Cerenkov Counter	Particle Identification

figure 2-1

the beam halo. The setup of these counters along with their dimensions is shown in figure 2-2.

2.3 Electronic Beam Definition

In order to minimize problems due to more than one particle passing through the apparatus at a time, an electronic definition of a beam particle was used. A particle was considered a good beam particle if the following conditions were satisfied: 1. within a 10 ns. period the M1,M2 and M3 counters all gave a signal ; 2. no signal was observed in the M1 counter during the 50 ns. before or the 50 ns. after the passage of the particle; 3. no signal was observed in the A0 counter either accompanying the particle or in the 50 ns. before or the 50 ns. after its passage; 4. the pulse height observed in the M1 counter was less than twice the size of the pulse expected from a minimum ionizing particle. The logic diagram of the electronics used to make these decisions is shown in figure 2-3.

2.4 The Veto System

All reactions in which a π^- interacts with a proton resulting in a neutron and a forward neutral meson have similar kinematics. For the momentum transfer region

BEAM DEFINING COUNTERS

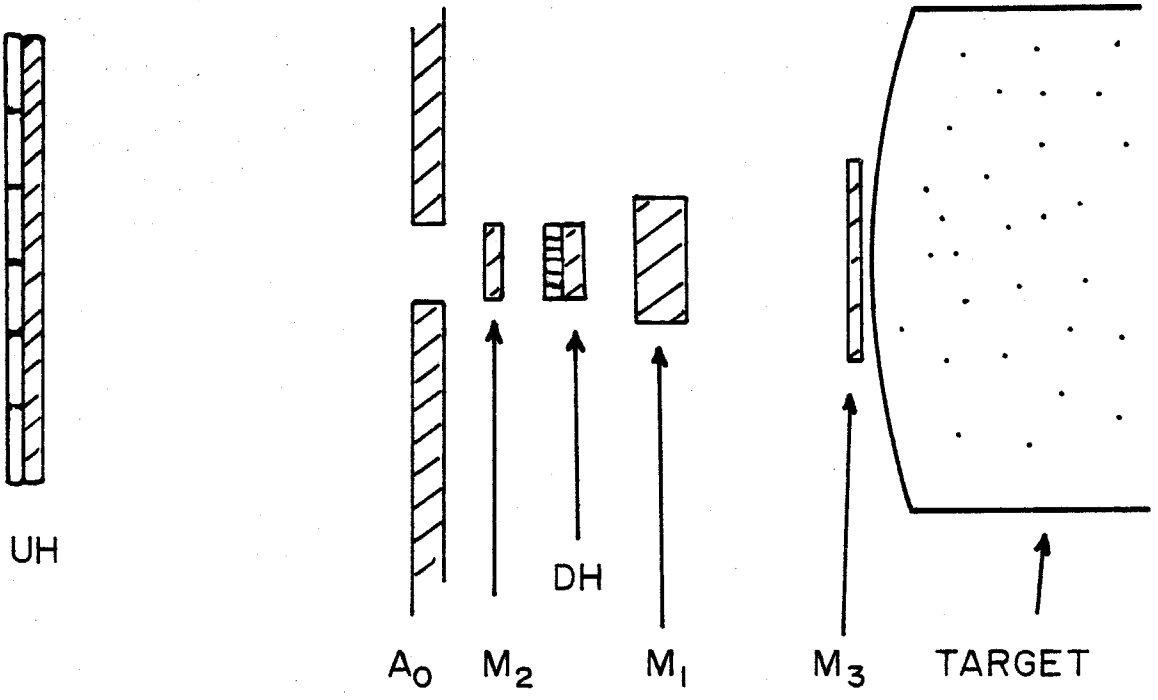

COUNTER	DESCRIPTION
UH	Upstream Hodoscope 6 elements in each view 2 3/4"L x 3/8"W x 1/8"T
DH	Downstream Hodoscope 6 elements in each view 1/2"L x 1/16"W x 1/8"T
A0	Beam Halo Anitcounter 14"Y x 17 3/4"X x 3/8"Z with a hole 3/8" x 3/8"
M1	Beam Telescope Counter 5/8"Y x 5/8"X x 1/4"Z
M2	Beam Telescope Counter 3/8"Y x 3/8"X x 1/8"Z
M3	Beam Telescope Counter 1" Diameter Circle 1/16" thick

figure 2-2

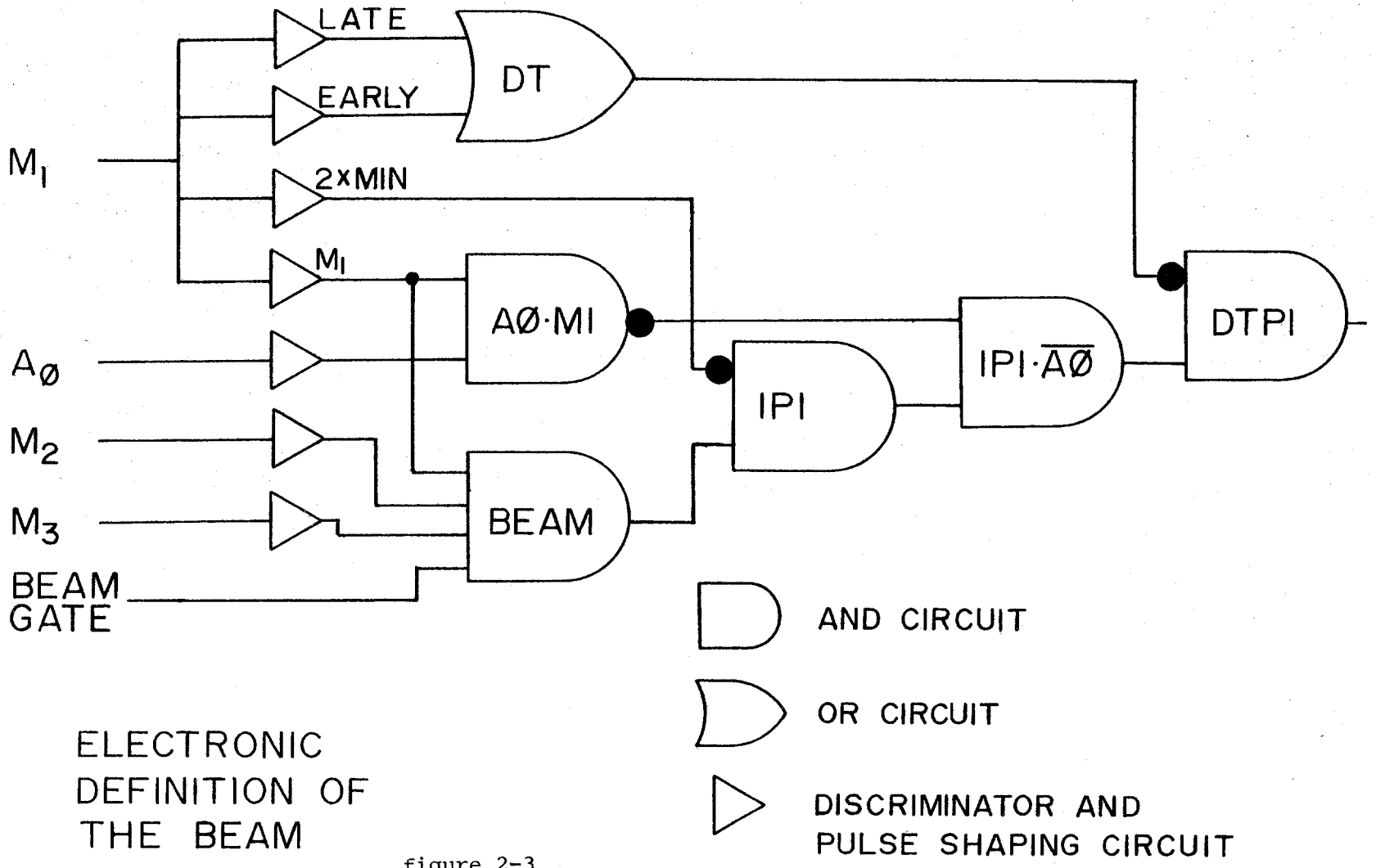

ELECTRONIC
DEFINITION OF
THE BEAM

figure 2-3

covered by this experiment, $-2\ GeV^2 < t < 0$, the kinetic energy of the neutron is less than 1 GeV and its angle is close to 90 degrees. Neutrons in this energy region are relatively difficult to detect. Rather than trying to detect them a veto system was built which detected charged particles and photons with a high efficiency but detected neutrons with a very low efficiency. Since the photons from the decay of the meson went forward most of the time, a good definition of the neutron meson final state is the requirement that no charged particles were detected and the only photons detected were in the forward direction.

This veto system consisted of a set of plastic scintillation counters surrounding the target to detect charged particles and a set of lead and plastic shower counters to detect those photons in the solid angle not covered by the photon detector. Schematic descriptions of the placement of these counters is given in figure 2-4.

2.5 The Neutral Final State Trigger

Since the neutral final state (NFS) cross section is only about ten times the charge exchange (CEX) cross section and has roughly the same energy dependence, it provides an effective means of rejecting most of the interactions which are not charge exchange. A trigger signal to indicate a

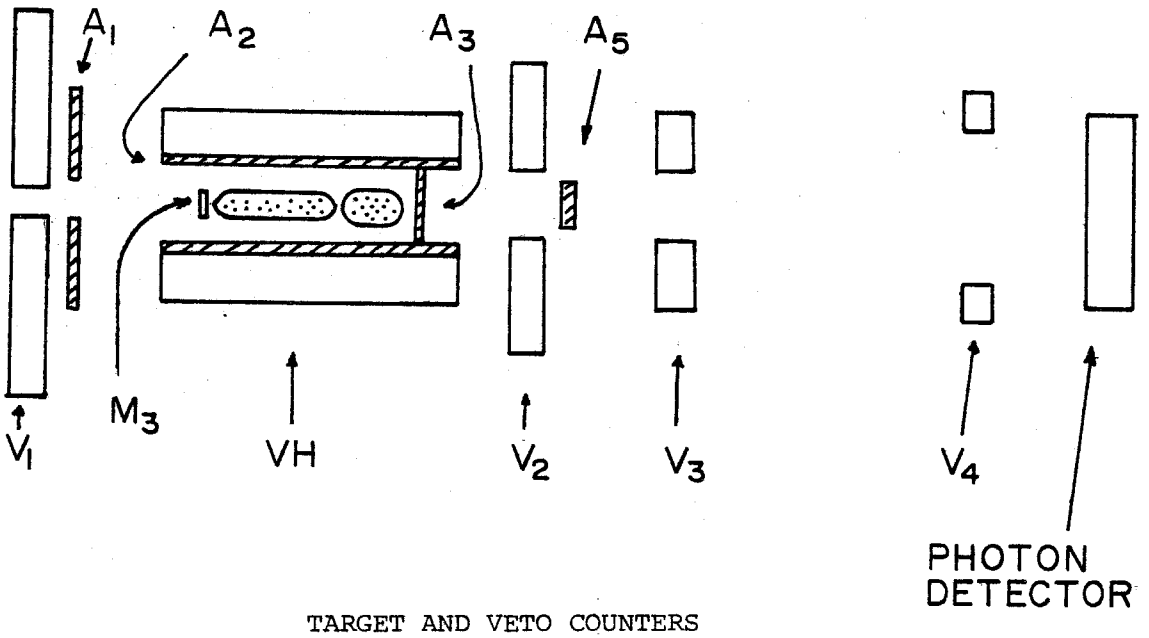

TARGET AND VETO COUNTERS

COUNTER	DESCRIPTION
V1	4 lead sandwich scintillation counters with 5 layers of lead each 1/4" thick
V2	4 lead sandwich scintillation counters with 5 layers of lead each 1/4" thick
V3	4 lead sandwich scintillation counters with 5 layers of lead each 1/2" thick
V4	4 lead sandwich scintillation counters with 5 layers of lead each 1/2" thick
VH	4 lead sandwich Cerenkov plastic counters with 1/8" layer of steel, 4 layers of 0.05" lead and 4 layers 1/4" lead

(continued on next page)

figure 2-4

COUNTER	DESCRIPTION
A1	2 counters each 1/4" thick which overlap to form a 10"Y x 20"X counter with a 1" square hole for the beam
A2	4 scintillation counters 7"Y x 3/8"X x 52"Z
A3	Scintillation counter 7"Y x 7"X x 1/4"Z
A5	Scintillation counter 4"Y x 4"X x 1/4"Z

figure 2-4 (continued)

neutral final state interaction was formed by electronically performing logic with signals from the beam definition electronics and the signals from the charged veto counters A1, A2, A3 and A5 as shown on the logic diagram in figure 2-5.

The A2 and A3 counters often had small signals due to delta rays. In order to study the effect of the A2 and A3 signal levels on the cross section measurement, these signals were pulse height analyzed and the discriminator thresholds on them in the trigger were set high enough to allow a small fraction of the minimum ionizing particles to pass through without making a discriminator output pulse. This loosening of the single charged particle threshold did not noticeably affect the trigger rate because the charge multiplicity of the charged states is usually high and always at least two.

Most of the veto system phototubes had occasional large pulses of duration greater than 100 ns. In order to insure no data were accepted while these phototubes were recovering, a veto signal was used in the trigger logic. Each of the phototube signals from the counters A2, A3, A5, V2, V3 and V4 were fed into comparitors which were set to produce an output as long as the input was above 20 millivolts. The output signals from these comparitors were

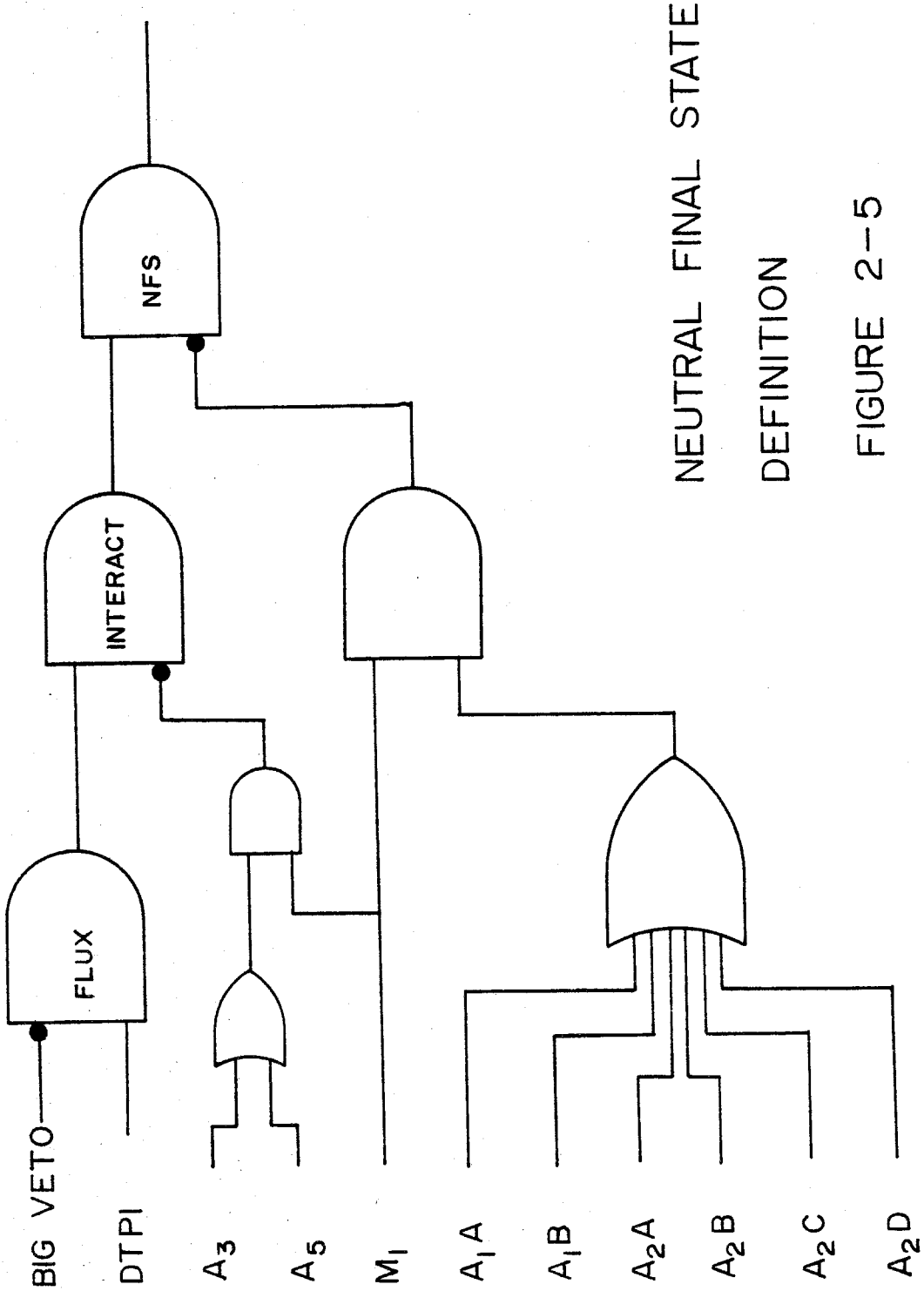

NEUTRAL FINAL STATE DEFINITION

FIGURE 2-5

mixed together and applied as a veto (BIG VETO) to the acceptable beam signal thus effectively turning off the apparatus until the tubes had recovered. The timing was such that an acceptable beam particle could not veto itself with the BIG VETO.

2.6 The Detector

To measure the positions and energies of the photons from reactions of the type

$$\pi^- + p \rightarrow \text{photons} + n$$

a photon shower detector was built. High energy photons interact with matter primarily through the pair production process. The electron and positron created lose energy by emitting photons through the bremsstrahlung process. The high energy bremsstrahlung photons in turn produce pairs forming more electrons and positrons. Thus a shower of electrons and positrons builds in intensity until the particles no longer have sufficient energy to make photons which have enough energy to produce pairs. This shower process has been studied both theoretically (reference 2-2) and experimentally (reference 2-3) by several authors. At photon energies above about a GeV the charged particles in the showers are distributed in a narrow cone centered on the

direction of the incident photon. The transverse projection of the shower intensity integrated over the longitudinal dimension, which is almost independent of the shower energy, has the shape shown in figure 2-6. Figure 2-7 shows the relative intensity of the shower as a function of the depth in the material at several energies.

In the past photon showers have been detected using many techniques. Lead glass (reference 2-4), sodium iodide (reference 2-5), wire chambers (reference 2-6), optical chambers (reference 2-7) and scintillation counters have all been used successfully but each has its limitations. Lead glass and sodium iodide have very good energy resolution but are expensive and hard to work with making it difficult to segment them sufficiently to give good position resolution. Wire chambers and optical spark chambers have good position resolution but have poor time and energy resolution. Plastic scintillation counters have fair energy resolution and, when constructed with segments on the order of the width of a photon shower, have better position resolution than wire chambers.

The shower detector is a stack of lead sheets in a lead holder with scintillation counters between the sheets to sample the shower intensity. Figure 2-8 schematically describes the detector. The lead sheets are 30"x30"x0.25"

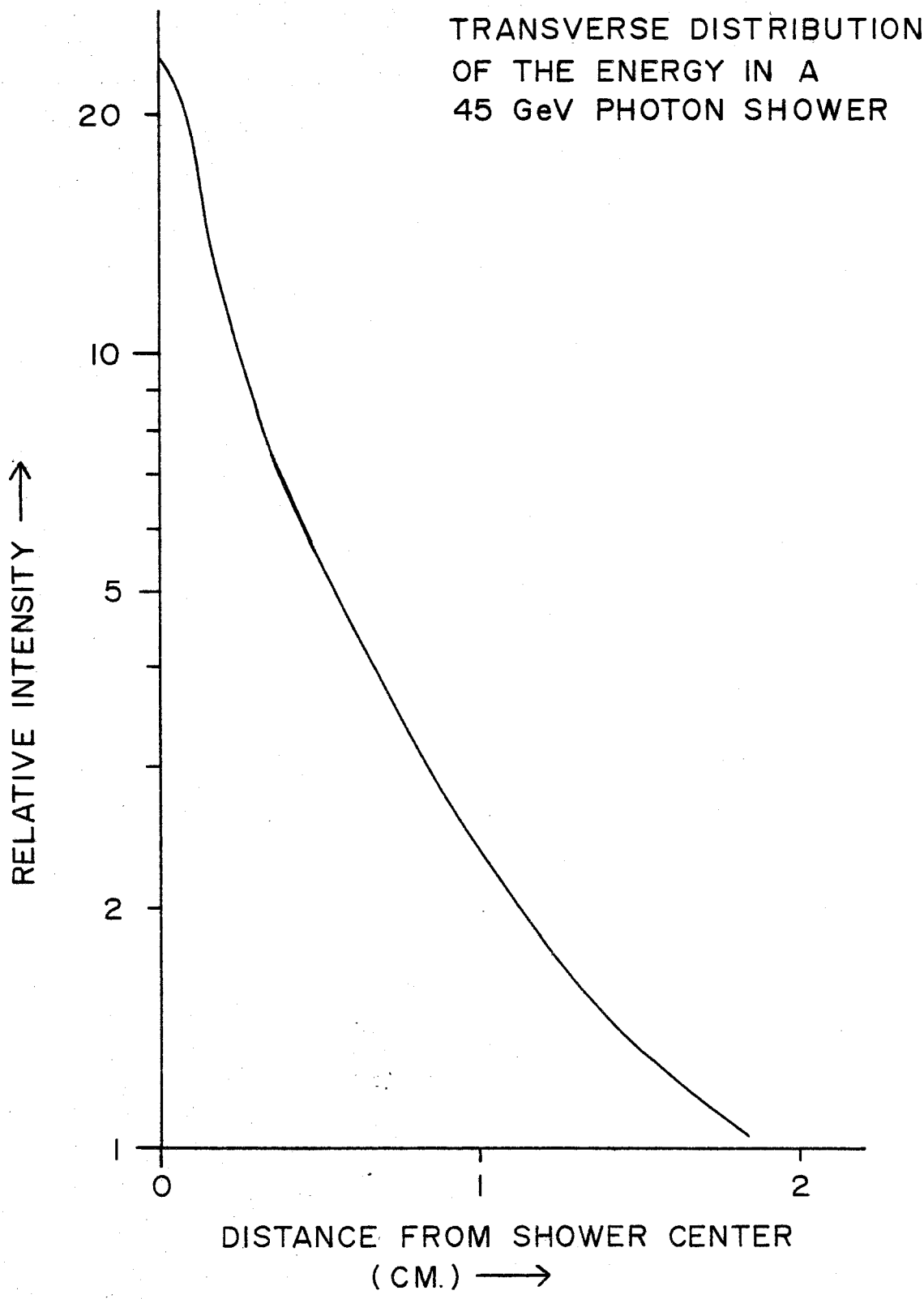
TRANSVERSE DISTRIBUTION
OF THE ENERGY IN A
45 GeV PHOTON SHOWER
20
10
5
2
1
RELATIVE INTENSITY ⟶
0
1
2
DISTANCE FROM SHOWER CENTER
(CM.) ⟶

figure 2-6

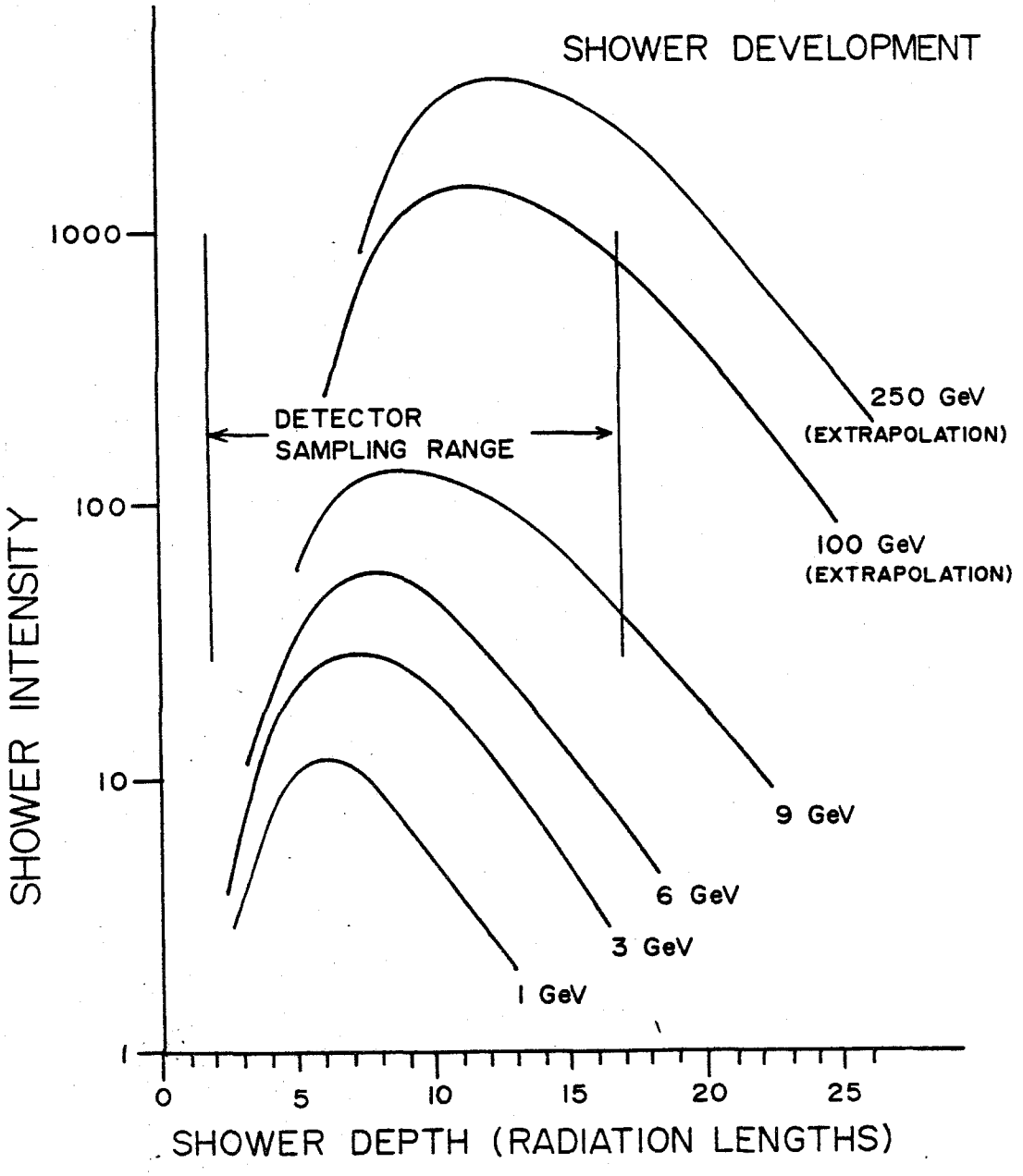
SHOWER DEVELOPMENT
1000
100
10
1
SHOWER INTENSITY
DETECTOR
SAMPLING RANGE
250 GeV
(EXTRAPOLATION)
100 GeV
(EXTRAPOLATION)
9 GeV
6 GeV
3 GeV
1 GeV
0
5
10
15
20
25
SHOWER DEPTH (RADIATION LENGTHS)

figure 2-7

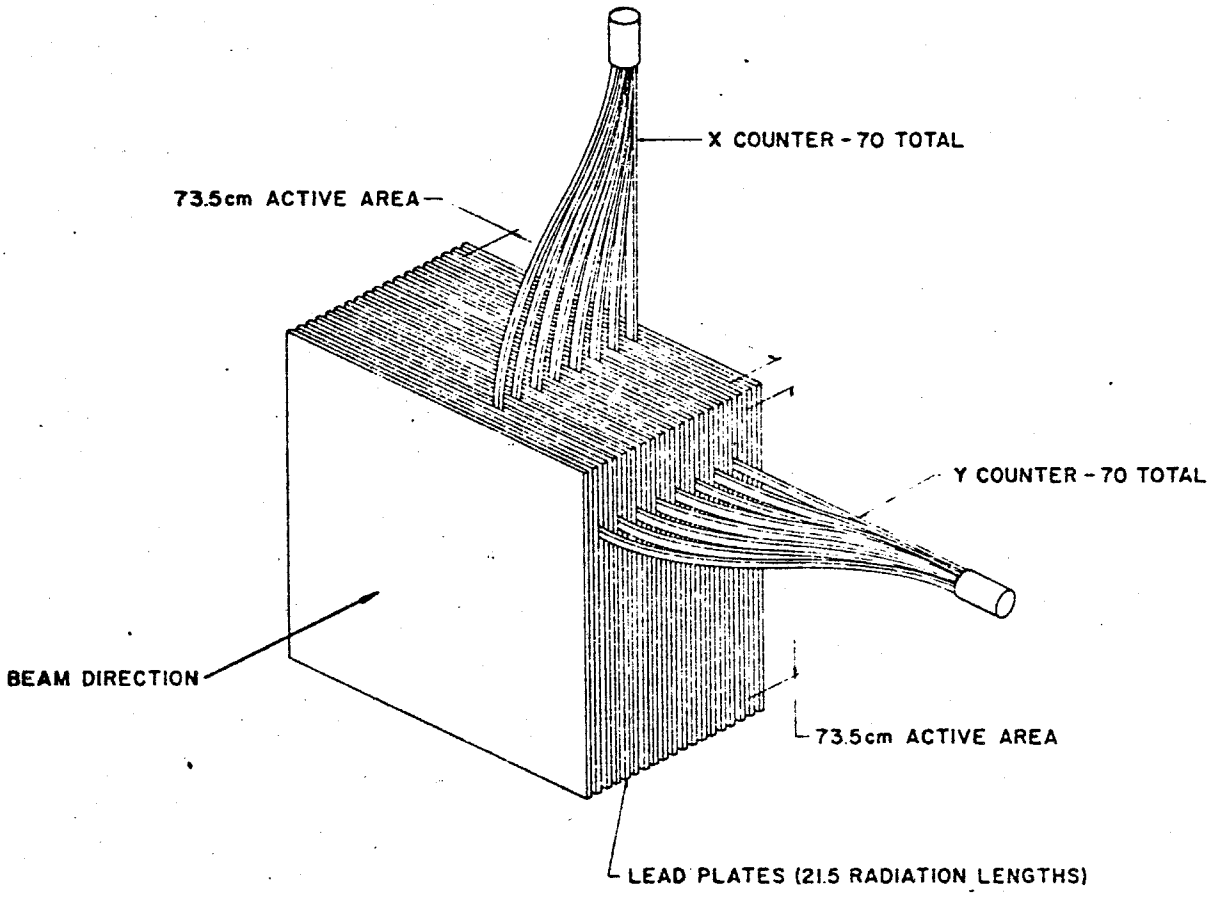

PHOTON DETECTOR

figure 2-8

lead antimony alloy. Each piece of scintillator plastic is Ø.25"xØ.41Ø"x32.". They are connected by light pipes in groups of 8 as shown in figure 2-9 to form the counters used to sample the shower intensity. This optical connection effectively integrates the shower in the longitudinal dimension. The detector has two sets of 7Ø such counters inserted into the lead holder to sample the shower in two orthogonal transverse views.

The construction of the individual counters made use of several tricks to reduce the attenuation along their length (reference 2-8). A yellow filter (Wratten No. 2E) was used to filter out the blue light which has a shorter attenuation length in the plastic. The counters were in optical contact with a black band which acted as an angle filter to stop that light which was being reflected up the counter at angles near the critical angle. Each of the 112Ø pieces of scintillator was wrapped with aluminized Mylar onto which a pattern of black lines had been silkscreened. The density of the lines in the pattern was varied from no lines far from the phototube end to solid black near the phototube end. These tricks produced counters whose light output, as measured by integrating the current pulses produced in an RCA 4517 phototube in response to an electron from a Ru^{106} source, was uniform to 3%. The pulse shape varied with position giving a 2Ø% increase in the voltage pulse

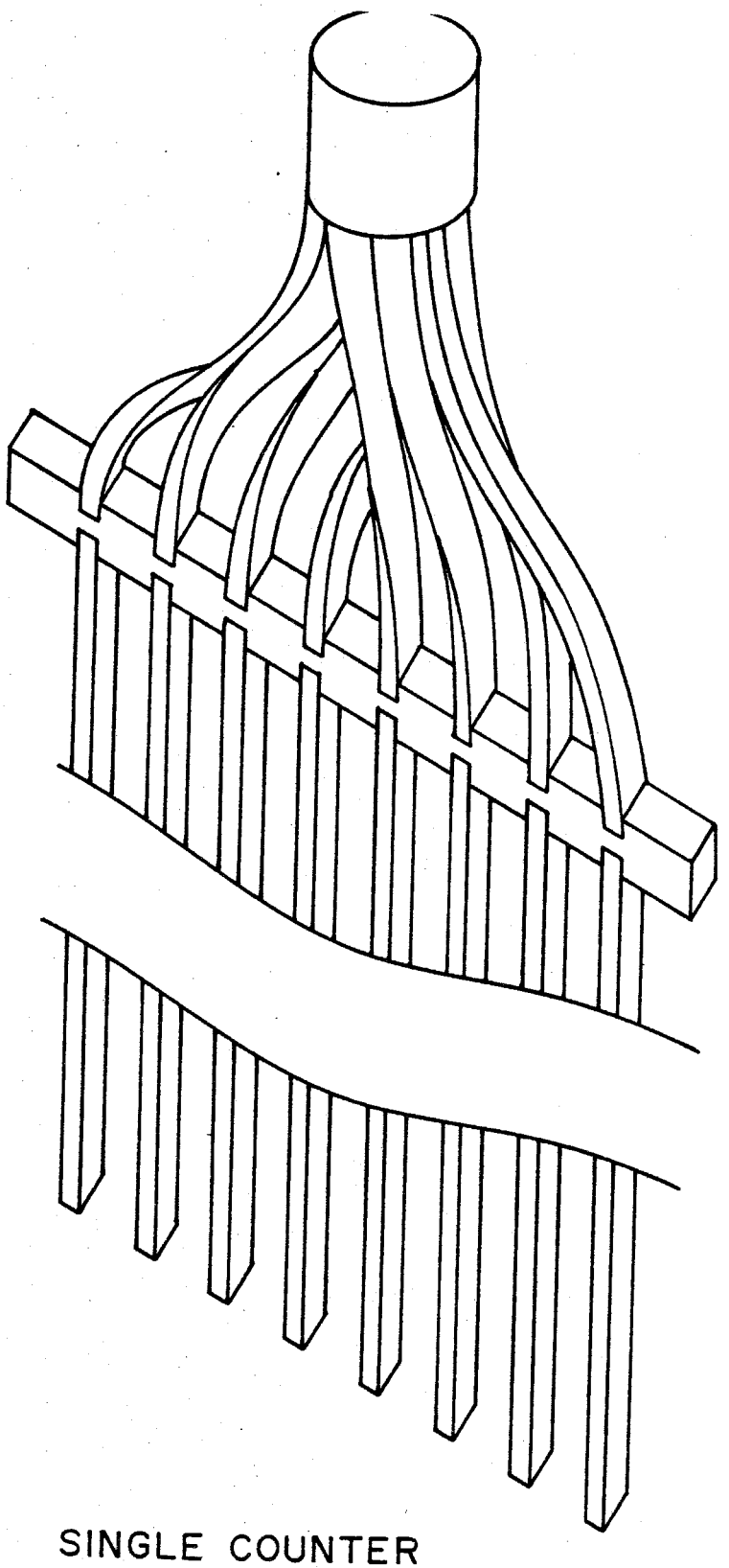

SINGLE COUNTER

height in going from the phototube end to the end away from the phototube.

In the completed detector each counter was connected to an RCA 4517 phototube which produced output signals about 10 ns. long. The signals from these tubes were input to analog to digital converters which, when triggered, digitized the charge collected from each tube during a 50 ns. gate. After digitization was complete the data were read by a Xerox Sigma 2 computer and written onto magnetic tape. The computer also analyzed a fraction of the data as it was collected to monitor the detector performance.

The detector was mounted on a motorized stand which could be moved vertically and horizontally to allow any of the counters to be centered on the beam. The gain of each counter was determined by centering that counter on the beam and measuring its response to electrons. During the experiment setup the gains of the phototubes were equalized by first determining the gains with an initial high voltage setting and then adjusting the high voltages according to the gain-voltage relation for the phototube and base configuration used.

The data from the detector consisted of 140 pulse heights. Figure 2-10 is a graphic representation of the

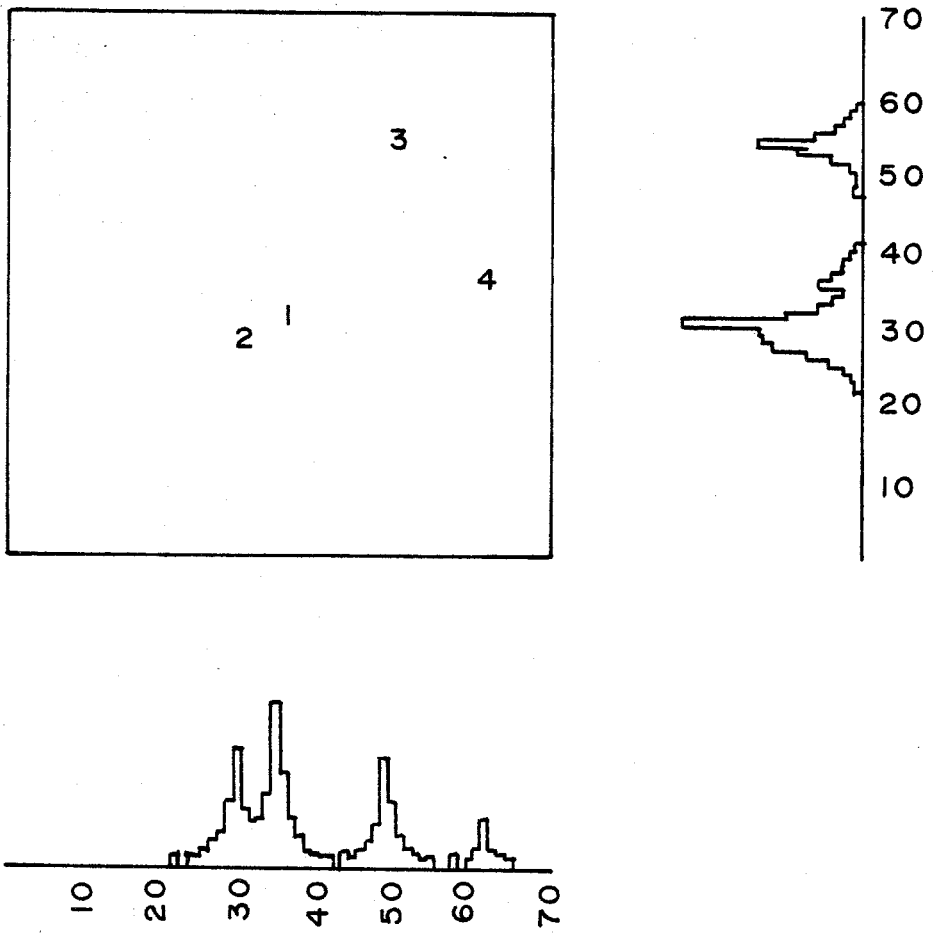

Graphic display of pulse height data

from the photon detector

figure 2-10

data from a typical event. The bar displays on the sides represent the data from the two views. The positions of the bars correspond to the positions of the counters and their lengths are proportional to the square root of the pulse heights observed in the counters. Two different techniques were used in analyzing these data. The moment technique, described in Appendix 1, involved no pattern recognition and was capable of determining the energy, position and effective mass of the photon system for each event. The other technique, described in Appendix 2, involved finding peaks in the two views and matching the information from the views to form a four vector for each photon. The latter technique gave much more information about the event than the moment technique but many of the events were too complicated to be completely reconstructed.

The energy resolution of the detector at low energies is dominated by the counting statistics involved in measuring the number of electron-positron pairs traversing the plastic scintillator. By comparing the detector response for minimum ionizing particles to its response for photon showers, it was found that the number of charged particles traversing planes of scintillator in 45 GeV showers was 60 ± 6 per GeV. Using this measurement and the assumptions that most of the charged particles traverse only one sheet of scintillator, that they are strongly correlated

in pairs and that the detector response is linear with energy, the detector energy resolution can be calculated to be

$$\Delta E/E = (0.182 \pm 0.009)/\sqrt{E}$$

where E is the energy in GeV
and ΔE is the RMS width.

This relation is in good agreement with the measured energy resolution.

At higher energies the resolution begins to be dominated by the gain setting errors. These errors are a constant fraction of the total energy in the shower. Combining this in quadrature with the energy dependent fractional error yields the form

$$\Delta E/E = \sqrt{a^2 + b^2}/E$$

where a is a gain variation term
and b is the energy dependent piece.

This formula breaks down at very low energies where some of the photons deposit a large fraction of their total

energy in a single piece of scintillator. In high energy showers only about 5% of the energy of the shower is deposited in the plastic scintillator of the detector. At energies so low that the electron positron pair can traverse only one plane of plastic, photons can deposit almost all their energy in a single plane and appear to have up to 20 times their true energy. The energy at which one would expect total absorption in a single plane works out to be in the range of 5 to 10 MeV. This energy is close to the minimum in the photon absorption cross section in lead. In the shower process there are many of these very low energy photons whose angles with respect to the shower are rather large. With this large number of large angle, long range photons present, one often deposits its energy at a large distance from the center of the shower. Their presence in the data can be inferred by comparing the pulse height distribution for peaks found in only one of the two planes to that for peaks found in both views. These distributions are both rather flat and agree well in both number and shape down to pulse heights corresponding to energies of about 180 MeV. Below this pulse height the distribution for peaks found in one plane rises sharply and achieves a level which is a factor of two greater than that for peaks found in both planes.

The position resolution for single photons is very

good. By looking at the distribution of the separation between the two photons from the decay of π^0's from the charge exchange reaction, this resolution and the beam energy can both be determined as described in section 4.4. The results of the position resolution measurement are shown in figure 2-11. These data were fit to the form

$$\Delta x = \sqrt{c^2 + d^2 / E}$$

where Δx is the position resolution

and a and b are parameters to be fit.

The best values for these parameters are c=0.313 mm. and d=2.96 mm$\sqrt{\text{GeV}}$. These can be understood as being due respectively to an error in the alignment of the counters and to the statistical fluctuations of the showers.

The position resolution for higher mass multiphoton states is dominated by the energy resolution. The centroid of the state is given by

$$\bar{X} = \sum_i E_i x_i \Big/ \sum_i E_i$$

where E_i is the energy of the i^{th}

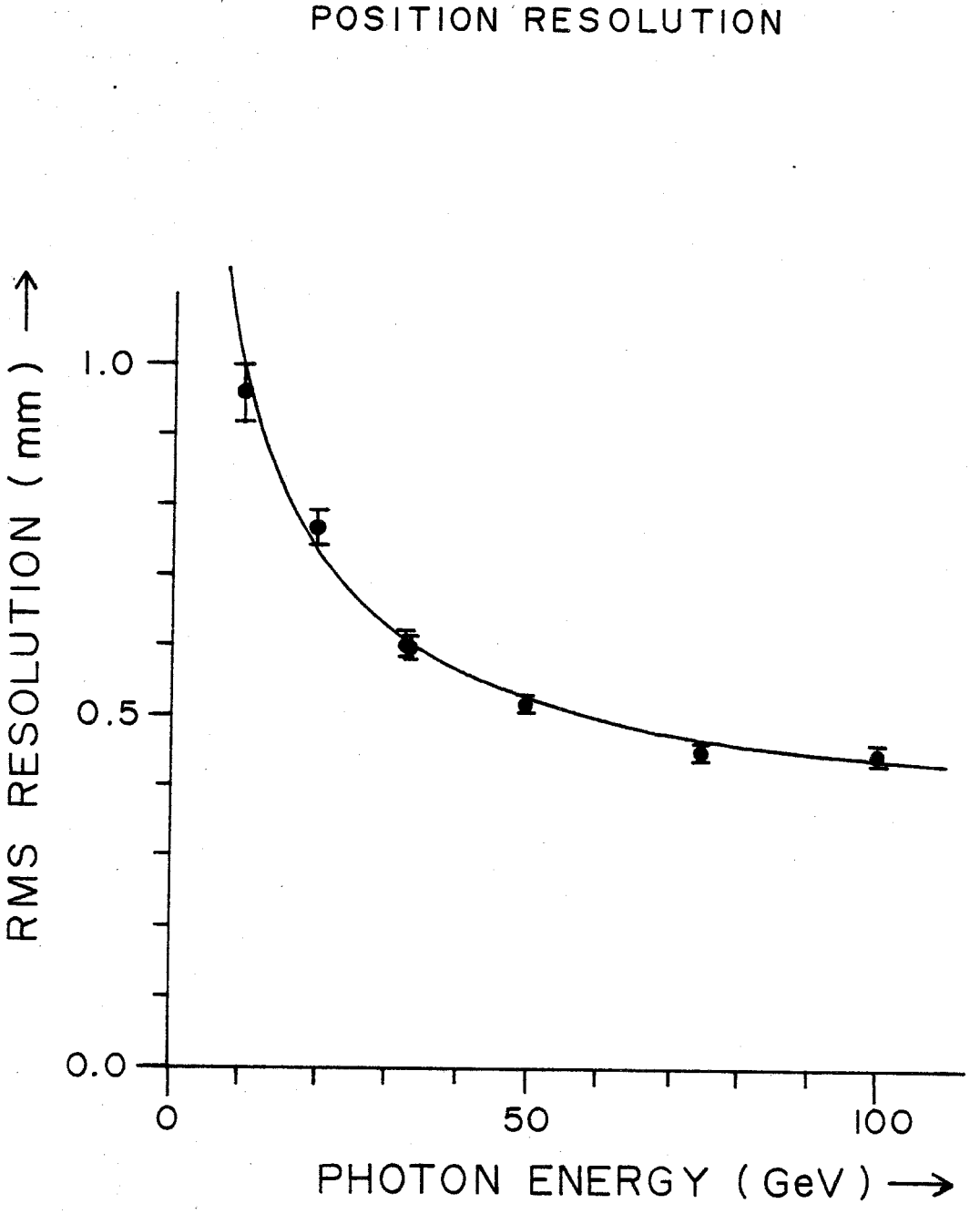
SINGLE PHOTON
POSITION RESOLUTION
RMS RESOLUTION (mm) ⟶
1.0
0.5
0.0
0
50
100
PHOTON ENERGY (GeV) ⟶

figure 2-11

photon.

and x_i is its position.

Errors in the energies and positions of the photons will cause errors in this centroid determination. When these resolutions are added in quadrature the overall resolution is bounded by

$$(\Delta x)^2 < c^2 + d^2/E + (a^2/2 + b^2/E)(m^2 L^2/E^2)$$

where c and d are the parameters for the position resolution,

a and b are the parameters for the energy resolution,

m is the mass of the decaying particle,

L is the distance between the target and the detector

and E is the energy of the particle.

For this experiment the π^o position resolution was about a millimeter at all energies while that for the η was about 4 millimeters.

The mass resolution of the detector is rather

complicated. It depends on the precise details of the decay kinematics. Using the parameterization of the energy and position resolutions described above the mass resolution for two photon events can be written

$$\left(\frac{\Delta m}{m}\right)^2 = \cos^2\theta\left(\frac{a^2}{2} + \frac{b^2}{E\sin^2\theta}\right) + \frac{E}{m^2L^2}\left(\frac{Ec^2\sin^2\theta}{2} + d^2\right)$$

where θ is the decay angle of the particle in the CM.

Values of the parameter a of around Ø.Ø6 give very good agreement with the measured π^o mass resolution.

3. The Data

The data were collected in many small runs, each a few hours in duration. For each run three types of information were recorded; hydrogen target data, scaler data and event data. The hydrogen target pressure and temperature were recorded by hand for each run.

The scaler data, which were recorded on magnetic tape with each event and at the end of each run, were the result of an electronic analysis performed on each particle passing through the apparatus while a run gate was on. The names and logical definitions of the recorded scalers are listed in table 3-1. Most of these were of interest only for monitoring purposes. Only the scalers FLUX, NFS, C FLUX and E FLUX were used directly in the cross section determination. The electronic definitions of FLUX and NFS are described in chapter 2. C FLUX was the subset of FLUX which also gave a signal in the Cerenkov counter and E FLUX was the subset of FLUX which deposited a large amount of energy in the detector. This latter quantity was useful in determining the erratically fluctuating electron fraction of the beam.

The event data, which were recorded on magnetic tape for each of the NFS triggers which occurred when the readout

TABLE 3-1

SCALER NAME	DEFINITION
BEAM	
ONEPI	
1PI AØ	
DTPI	
FLUX	
NFS	
GOBITS	Particles which satisfied the neutral final state conditions and occured when the bit setting electronics were active
TRIGGER	Particles which satisfied the GOBITS definition and occured while the computer wasn't busy.
C FLUX	Particles satisfying the electronic FLUX definition and having a signal in the Cerenkov counter.
E FLUX	Particles satisfying the electronic FLUX definition and having a sum of the signals from the detector counters nearly as large as the sum corresponding to the full beam energy.

Names without definitions are defined in the electronics diagrams of figures 2-3 and 2-5.

system was not busy, consisted of the pulse heights in each of the 140 detector counters; the detector position; pulse heights from the A2, A3, VH, V2, V3, V4 and and Cerenkov counters; and bits from the electronic analysis for the VH, V1, V2, V3, V4, Cerenkov and hodoscope counters. In addition, for each of these events a run number, event number, date and time were recorded.

4. Reaction Independent Analysis Details

Due to the similar nature of the final states studied, many of the techniques and corrections involved in the analysis of the different reactions are very similar. This chapter describes some of the details of these techniques and corrections. All correction factors are calculated as efficiencies so the relation between the true cross section and the uncorrected measured cross section is

$$\sigma = \sigma_m / (\text{correction factor}).$$

4.1 Delta Rays

When charged particles pass through matter they lose energy by several processes the most important of which is ionization of the matter. In the ionization process some electrons are knocked out with energies high enough to escape from the hydrogen target. These escaping electrons, known as delta rays, deposit energy in the charged particle veto counters A2 and A3. They do not significantly degrade the energy of the beam particles, but they do cause otherwise good events to be rejected.

The spectrum of the energy deposition in the veto counters can be calculated from the known cross sections and

the measured range energy relationships. For the kinematic region of interest here the number of delta rays expected per unit path length and unit energy is

$$d^2N/dEdx=C/E^2,$$

where E is the delta ray energy
and C is a constant which in hydrogen is Ø.154 MeV cm^2/gram.

Since delta ray energies are very large compared to atomic binding energies their production can be viewed as elastic scattering between the electrons and the incident beam particles. Thus the scattering angle is constrained by energy and momentum conservation. In our range of energies the angle is very well approximated by

$$\Theta = \sqrt{2m/E}\,.$$

These formulas along with "Feather's Rule" (reference 4-1) for the electron range energy relationship and a detailed knowledge of the matter distribution in the target and veto system were used to calculate the energy deposition in the veto counters. These were combined with the measured counter attenuations and gains to predict the pulse height spectrum expected from delta rays.

To check the calculation, the delta ray spectrum from particles traversing the entire target length was calculated and compared to the measured spectrum from straight through beam particles. For the pulse height cutoff used in analyzing the data the correction factor for the neutral final state was between 0.90 and 0.92 depending on the target configuration.

4.2 Neutral Veto System Inefficiency

Since the neutral veto system was not 100% efficient at rejecting photons, a correction had to be made to compensate for accepting final states with a fast neutral meson in the forward direction and an excited baryon or slow meson in the target. The photon detection efficiency is poorest for low energy photons. This indicates the $\Delta^{\circ}(1236)$ decay into π° and neutron will be one of the most troublesome backgrounds. A Monte Carlo calculation (reference 4-2) using the measured counter efficiencies (reference 4-3) indicates that 1.6% of the Δ° to π° neutron decays are misidentified as being just neutrons. If events with a good π° in the detector and photons in the VH veto counter and no photons in the other counters are all assumed to be Δ° decays, and assuming 1.6% of these are misidentified as just neutrons, then the correction factor would be about 1.015. Since many of these events are from more massive

baryons with higher energy photons in their decay scheme, which make them easier to detect, the correction factor should be lower than the 1.Ø15 arrived at above.

Another estimate (reference 4-4) of the neutral veto inefficiency can be arrived at by looking at events rejected by only one of the veto counters. This estimate also includes the effect of accidental noise pulses in the counters. This scheme yielded a correction consistent with the one above. The correction factor used for the data analysis was $1.Ø13 \pm Ø.Ø1$.

4.3 Neutron Detection

Both the neutral and charged veto systems had a small but not negligible efficiency for detecting the recoil neutron in the reactions being studied. These efficiencies depend on the neutron energy and angle. As a result the correction is slightly different for the different values of t and varies from reaction to reaction. The neutron detection efficiencies for the A2 and VH counters were measured (reference 4-5) in a tagged neutron beam at the Berkeley 184" cyclotron as a function of both energy and angle. As a check of these measurements, the data were analyzed to look for the effect of neutrons in these counters. A sample of events was selected which had all the

characteristics of charge exchange events except for the signals from the A2 and VH counters in the direction of the recoil neutron. These events were then used to measure the neutron efficiencies of the counters. This check agreed well with the earlier A2 efficiency measurement but disagreed with the original VH measurement. As a compromise the neutron correction for the VH counter was taken to be the average of the two determinations with an error in the correction large enough to be consistent with either. This was one of the larger contributions to the overall systematic error of the experiment.

4.4 Beam Energy Determination

As mentioned in chapter 2 the beam energy, although stable, was not well known, at the time the data were collected. A knowlege of the beam energy is important, not only for measuring the energy dependence of the cross section, but also for getting the proper normalization of the momentum transfer scale. Since the beam momentum dispersion was narrower than the energy resolution of the detector, the beam energy was used in the calculation of t. For the charge exchange reaction the differential cross section varies with momentum transfer, t, so rapidly that at a t of $-0.35\ GeV^2$ a 1% change in the beam energy value makes a 10% change in the measured differential cross section.

The beam energy for each operating configuration of the experiment was determined by studying the distribution of separations between the two photons in events which satisfied the η neutron final state requirements. The separation between the photons from a two photon decay of an extremely relativistic particle is

$$S = Smin/\sin\theta$$

where Smin is $2m^2 L/E^2$,
L is the distance from the target to the detector,
m is the decaying particle mass,
E is its energy,
and θ is the center of mass decay angle.

Since the π^o and η are spinless particles, their decays are isotropic in the center of mass implying a uniform distribution in $\cos\theta$. Thus the distribution of separations in decays should be

$$dN/dS = A/[Smin(S/Smin)^2\sqrt{(S/Smin) - 1}\,],$$

where A is just a normalization constant. The observed distribution is modified due to the finite target length, the beam momentum dispersion, and the single photon position resolution of the detector. When these are accounted for the separation distribution becomes

$$\frac{dN}{ds} = \frac{A}{\sigma}\int_{L_1}^{L_2} dL \int_{E_1}^{E_2} \frac{dE}{S_{min}} \int_{S_{min}}^{\infty} ds' \; \frac{e^{-\frac{(S-S')^2}{4\sigma^2}}}{\left(\frac{S'}{S_{min}}\right)^2 \sqrt{\left(\frac{S'}{S_{min}}\right)^2 - 1}}$$

where σ is the single photon position resolution at half the beam energy,

E_1 and E_2 are the lower and upper limits of the beam energy spread,

L_1 and L_2 are the distances to the near and far ends of the target,

and A is the normalization.

Although the beam energy was not known its fractional spread was known as were the distances to the target ends. Their distributions were also known to be approximately flat. The π^0 and η separation distributions for each

running configuration were fit to this form allowing the beam energy and the detector position resolution to vary. The distributions and fits for the 20 GeV and 150 GeV data sets are shown in figure 4-1 and those for the are shown in figure 4-2. Table 4-2 gives the results for each of the fits.

4.5 Detector Gains

The gains of the detector photomultiplier tubes varied during the collection of data for each energy. To partially correct for this problem the 's from charge exchange events were used as a monoenergetic source to determine the gains. The procedure used was as follows: for each counter charge exchange events were selected which had both photons from the decay in that counter; the average pulse height from the counter for those events was determined and a correction factor was calculated, which, when multiplied by the average, would give the pulse height desired for a beam energy . Since the charge exchange cross section is peaked strongly in the forward direction, only those counters near the center of the detector (X26-X43 and Y26-Y43) could be corrected in this fashion. This technique only corrected the gain of a counter averaged over an entire energy setting, any fluctuations occurring during that time were corrected for only by this averaging.

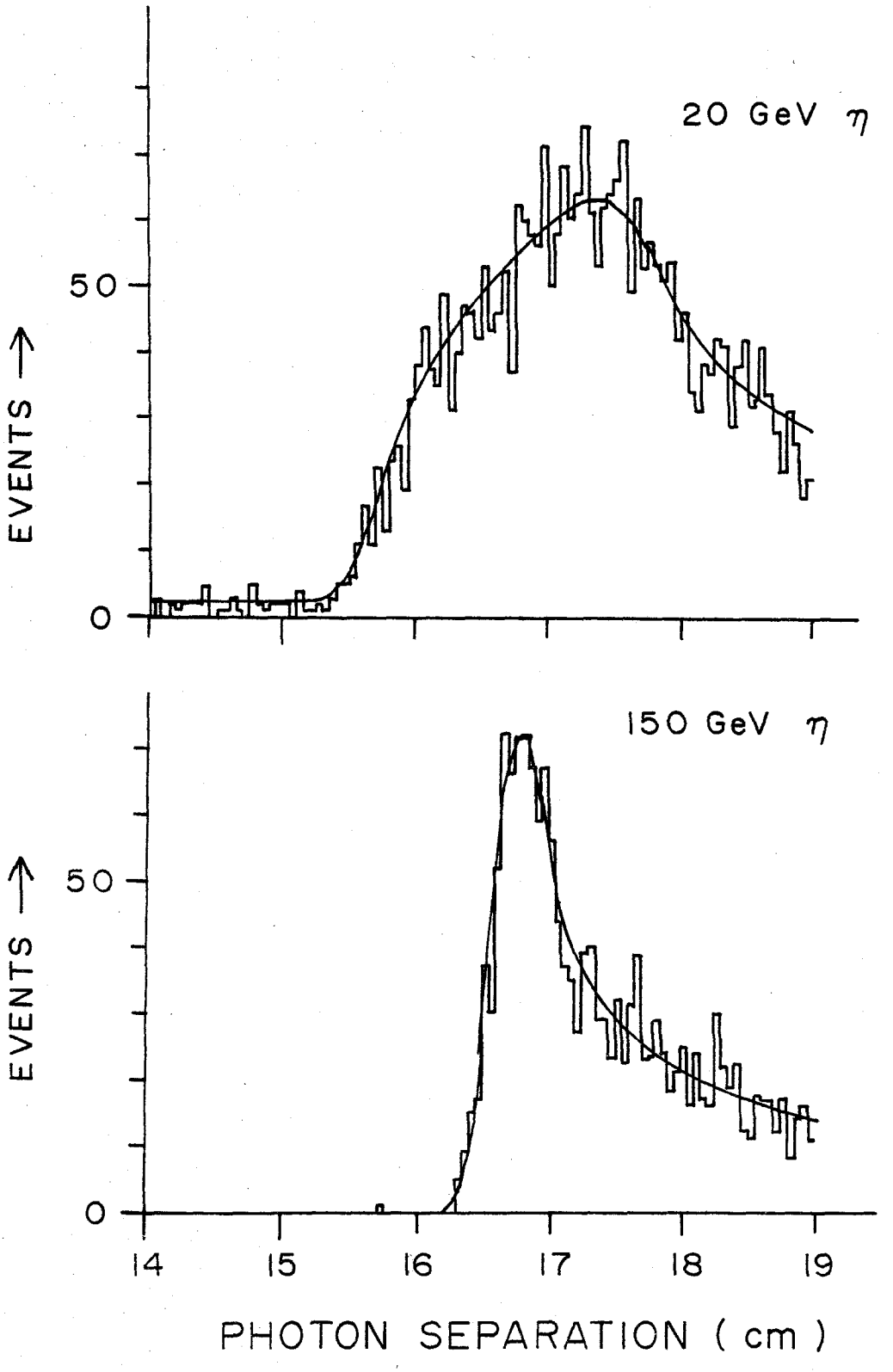
20 GeV η
150 GeV η
EVENTS →
EVENTS →
50
0
50
0
14
15
16
17
18
19
PHOTON SEPARATION (cm)

figure 4-1

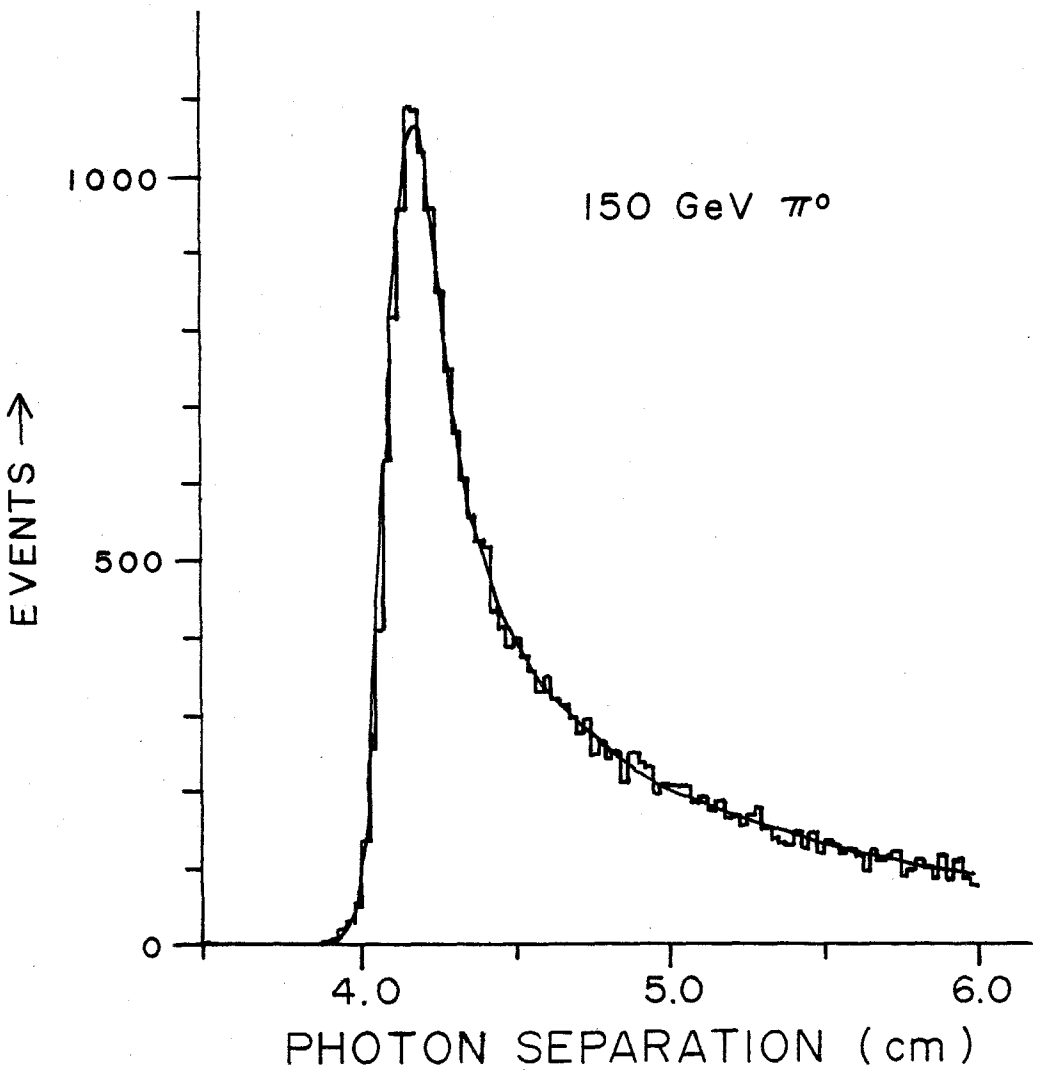

figure 4-2

TABLE 4-1

Data Set	Energy from Fit to η (GeV)	Position Resolution from Fit to π^0 (mm)
20	20.75 ± 0.03	0.95 ± 0.05
40a	40.96 ± 0.05	0.77 ± 0.03
40b	41.28 *	*
65a	66.06 ± 0.09	0.61 ± 0.02
65b	65.05 ± 0.07	0.59 ± 0.02
100	100.78 ± 0.07	0.52 ± 0.01
150	150.55 ± 0.10	0.45 ± 0.01
200	199.83 ± 0.14	0.45 ± 0.01

* This data set, which had a mix of running target configurations, failed to give an acceptable fit. The energy was determined by looking at the front edge of the separation distribution.

A different scheme for the gain determination was used in the analysis of the multiphoton events. This scheme used the two independent measurements of the total energy provided by the two views. It was iterative and proceeded as follows: the gains in one of the views were fixed while those in the other were varied to minimize the average over the events of the square of difference between the views; the roles of the views were reversed and the square of the difference again minimized. To keep the scheme from driving the gains all to zero, the average of the x view was renormalized to one at each iteration step. This scheme used all the recorded data for which the discrepancy between the views wasn't greater than five standard deviations, thus dramatically increasing the statistical precision of the determination.

In later experiments with the same detector we developed a monitoring scheme which allowed us to monitor the gains at half hour intervals during the data taking.

4.6 The Normalization

The errors in the normalization of the charge exchange reaction cross sections are dominated by systematic uncertainties in the corrections and the uncertainties in the hydrogen density. To minimize instrumental effects,

data which were accumulated during stable periods of operation were selected for use in determining these integrated cross sections. These data were analyzed, as described in chapter 5, to determine the number of charge exchange events. The number of incident π^-'s was calculated using the scaler data from the runs. To first order this was just C•FLUX but it had to be corrected for electron and muon contamination. The muon fraction was taken to be a constant fraction of the pion flux while the electron fraction was determined from the scaler quantities FLUX and E•FLUX. The complete data set was used in the determination of the differential cross sections in all the reactions.

For the other final states the data were normalized to the charge exchange cross section. This allowed the full data set to be used in these integrated cross section determinations rather than just the data collected during stable periods of operation. This greatly enhanced the statistical precision of these measurements.

4.7 Data Selection

All the reactions presented here are pion induced and have a neutron and a meson decaying into photons in the final state. Prior to the analysis of the detector

information all the data were subjected to selection criteria to insure the pion induced neutron final state. These criteria were: the Cerenkov counter identified the beam particle as a pion; none of the counters in the neutral veto system gave a signal; and the pulse heights in the charged veto counters A2 and A3 were less than a cutoff which was chosen to be well below the pulse height expected from minimum ionizing particles.

5. The Two Photon Final State Analysis And Data

The π°, η and η' mesons all have two photon decay modes, which makes the analysis of these reactions very similar. For the integrated reaction cross sections the analysis was based on the moment technique, described in appendix 1, supplemented by a simple peak counting scheme. The counting scheme used the relative energies of the peaks to determine the cosine of the decay angle in the center of mass for each two peak event. Four criteria had to be met before an event was included in the data sample: the event had to pass the criteria for a pion induced neutron final state event as defined in section 4.7; the peak counting scheme had to indicate two and only two peaks had been found; the absolute value of the cosine of the center of mass decay angle had to be less than 0.7; and the mass and energy of the event were required to fall in a hand drawn region of the mass energy scatter plot. To illustrate the quality of the charge exchange data, figures 5-1 and 5-2 show the distributions in mass and energy and figure 5-3 shows the mass-energy scatter plot with the hand drawn region of acceptance for the 100 GeV data.

For the differential cross section the analysis used the moments method for event selection but used the fitting technique, described in appendix 2, to determine the

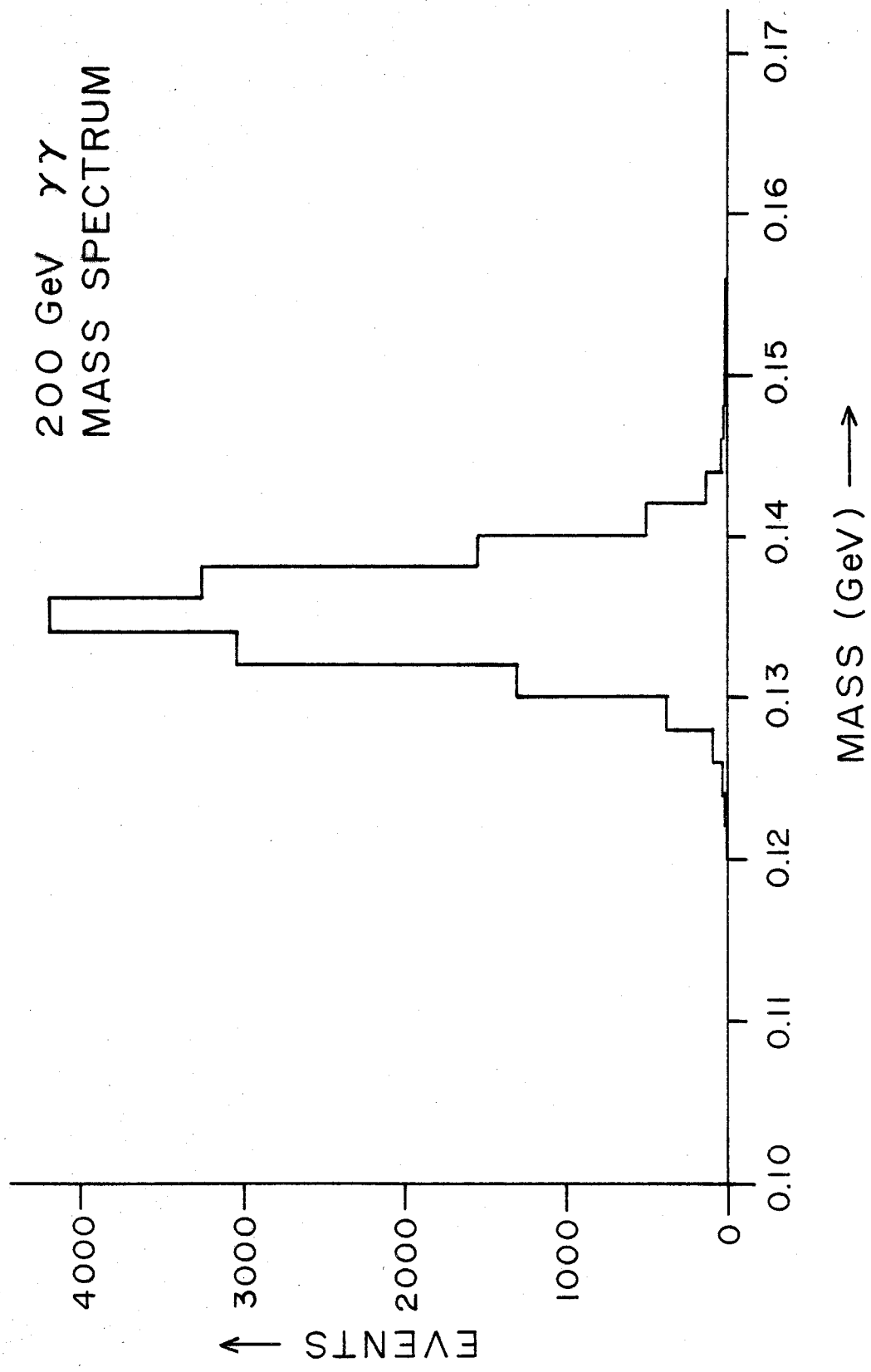
200 GeV γγ
MASS SPECTRUM
EVENTS
4000
3000
2000
1000
0
0.10
0.11
0.12
0.13
0.14
0.15
0.16
0.17
MASS (GeV)

figure 5-1

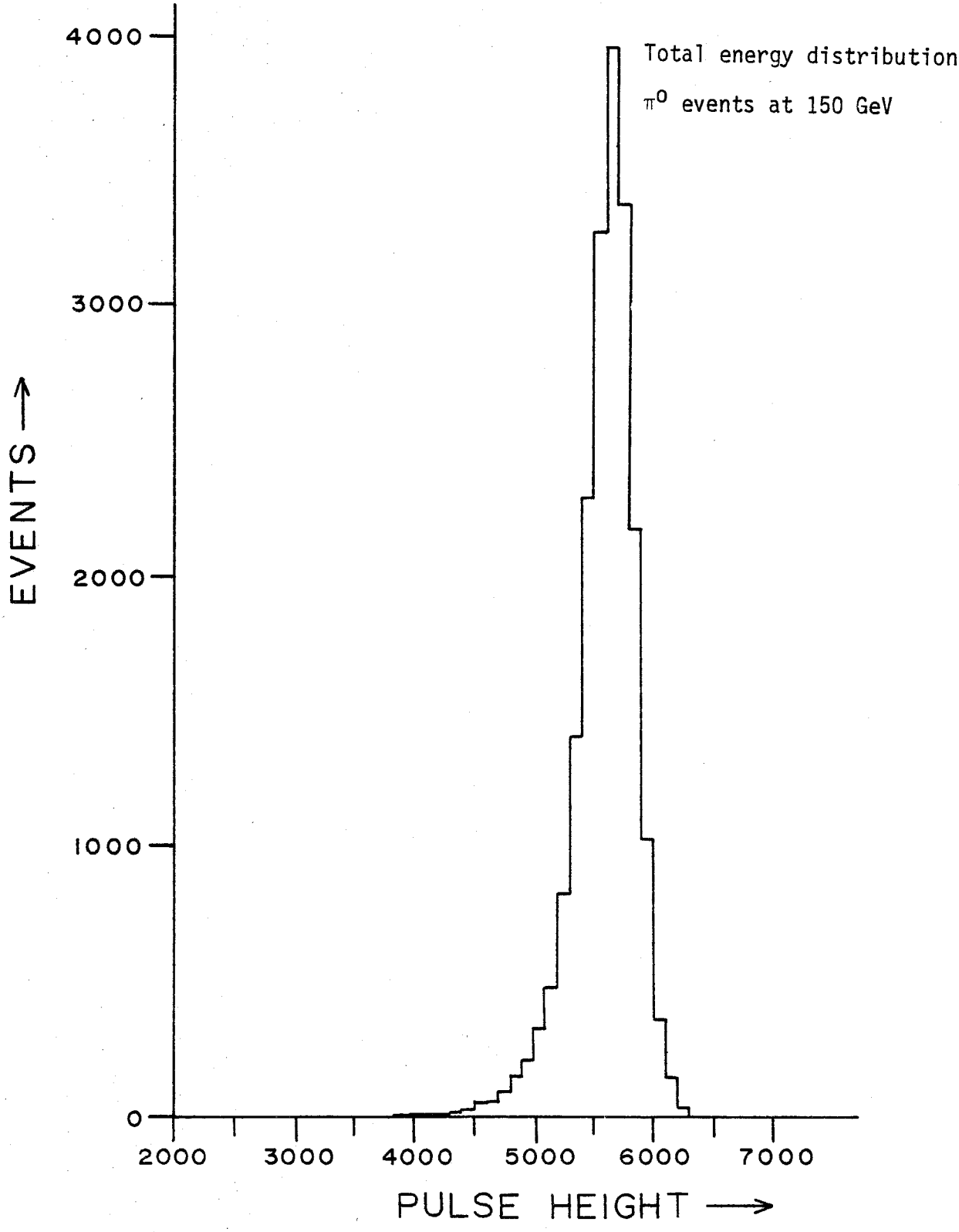
Total energy distribution
π^0 events at 150 GeV
EVENTS
4000
3000
2000
1000
0
2000
3000
4000
5000
6000
7000
PULSE HEIGHT

figure 5-2

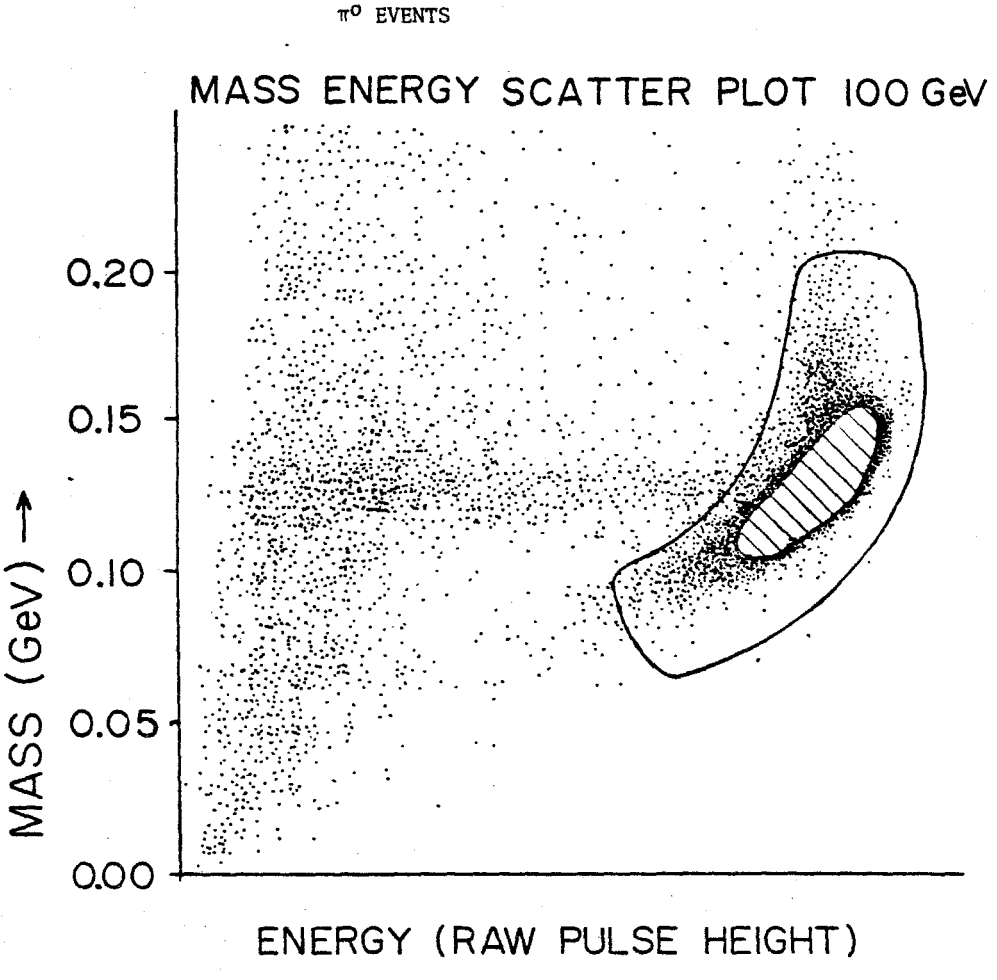
π^0 EVENTS
MASS ENERGY SCATTER PLOT 100 GeV
0.20
0.15
0.10
0.05
0.00
MASS (GeV) →
ENERGY (RAW PULSE HEIGHT)

figure 5-3

kinematic quantities for the event. The fitting technique gave better mass and position resolution than the moments technique, but a fraction of the data had to be excluded due to failures in the fitting procedure. Those events passing the moments selection criteria, which were successfully fitted and had good hodoscope data, were included in the sample of events for the differential cross section determination. Those events which failed to give good fits were analyzed using the moments technique. The distributions of the failing events were statistically indistinguishable from those of the events successfully fit when they were also analyzed with the moment technique. For the events in the higher energy data sets. the t for the events was calculated using the approximation

$$t=E^2 r^2/L^2$$

where E is the beam energy,
r is the distance between the measured particle position and the position of the projected onto the detector as determined by the hodoscope data
and L is the distance from the target to the detector.

At 20 and 40 GeV the distance from the target to the detector was so small, relative to the target length, that the measured mass gave a better determination of the distance from the decay vertex than just the distance to the target center. The calculated mass is given by

$$m^2 = E^2(E_1 E_2 Sep^2)/[L^2(E_1+E_2)^2]$$

where E_1 and E_2 are the energies of the two photons

and Sep is the separation between them.

Using this in the approximation for t yields the relationship

$$t=(E_1+E_2)\, m^2 r^2/[E_1 E_2 Sep^2],$$

which was used for the 20 and 40 GeV data.

The differential cross sections for the charge exchange reaction are given in table 5-1. They have been corrected for the experimental t resolution and bin width. The t resolution is discussed in detail in appendix 3. The corrections needed were determined by studying how an empirical function was affected when smeared by the experimental resolution and binning. The empirical function

$-t$ (GeV^2)	Bin Width (GeV^2)	Beam Momentum GeV						$\alpha^*(t)$
		20.8	40.8	64.4	100.7	150.2	199.3	
0.002	0.004	104 ± 5	50.6 ± 2.1	32.0 ± 1.3	20.3 ± 0.8	13.4 ± 0.5	10.4 ± 0.4	0.491 ± 0.012
0.006	0.004	105 ± 5	57.8 ± 2.3	35.9 ± 1.4	21.1 ± 0.8	14.0 ± 0.6	10.1 ± 0.4	0.474 ± 0.011
0.012	0.008	121 ± 5	55.2 ± 1.8	34.5 ± 1.1	20.8 ± 0.7	14.6 ± 0.5	11.0 ± 0.4	0.474 ± 0.010
0.020	0.008	120 ± 5	59.9 ± 1.9	36.8 ± 1.2	21.5 ± 0.7	14.8 ± 0.5	11.3 ± 0.4	0.471 ± 0.009
0.028	0.008	137 ± 5	62.1 ± 1.9	36.9 ± 1.2	22.6 ± 0.7	15.6 ± 0.5	11.3 ± 0.4	0.453 ± 0.009
0.040	0.016	134 ± 4	62.1 ± 1.6	37.0 ± 1.0	22.1 ± 0.6	14.5 ± 0.4	10.6 ± 0.3	0.439 ± 0.008
0.056	0.016	126 ± 4	59.0 ± 1.6	36.5 ± 1.0	20.5 ± 0.6	13.2 ± 0.4	9.3 ± 0.3	0.422 ± 0.008
0.072	0.016	116 ± 4	54.2 ± 1.5	30.7 ± 0.9	18.6 ± 0.5	11.9 ± 0.3	8.84 ± 0.26	0.427 ± 0.008
0.090	0.020	108 ± 3	48.0 ± 1.2	28.4 ± 0.8	16.1 ± 0.4	10.0 ± 0.3	6.86 ± 0.20	0.393 ± 0.007
0.110	0.020	92.1 ± 3	40.1 ± 1.1	22.9 ± 0.6	12.9 ± 0.4	8.2 ± 0.2	5.79 ± 0.18	0.387 ± 0.008
0.140	0.040	74.3 ± 2.1	31.4 ± 0.8	17.0 ± 0.4	9.5 ± 0.2	5.54 ± 0.15	3.88 ± 0.11	0.344 ± 0.007
0.180	0.040	50.9 ± 1.5	20.2 ± 0.5	10.6 ± 0.3	5.87 ± 0.17	3.54 ± 0.11	2.40 ± 0.08	0.326 ± 0.008
0.220	0.040	33.7 ± 1.2	13.1 ± 0.4	6.8 ± 0.2	3.64 ± 0.13	2.10 ± 0.08	1.36 ± 0.06	0.294 ± 0.010
0.260	0.040	22.0 ± 0.9	7.6 ± 0.3	4.20 ± 0.18	1.93 ± 0.09	1.15 ± 0.06	0.709 ± 0.040	0.248 ± 0.012
0.310	0.060	11.6 ± 0.5	4.24 ± 0.18	2.09 ± 0.10	0.99 ± 0.05	0.53 ± 0.03	0.311 ± 0.022	0.208 ± 0.013
0.370	0.060	4.8 ± 0.3	1.73 ± 0.11	0.75 ± 0.06	0.37 ± 0.03	0.204 ± 0.019	0.117 ± 0.013	0.184 ± 0.020
0.450	0.100	1.44 ± 0.13	0.50 ± 0.04	0.199 ± 0.023	0.088 ± 0.011	0.050 ± 0.007	0.026 ± 0.005	0.123 ± 0.031
0.550	0.100	0.44 ± 0.07	0.090 ± 0.018	0.058 ± 0.012	0.022 ± 0.006	0.0067± 0.0027	0.0071± 0.0026	0.040 ± 0.067
0.650	0.100	0.36 ± 0.06	0.103 ± 0.018	0.044 ± 0.010	0.015 ± 0.004	0.0067 ± 0.0024	0.0091 ± 0.0026	0.052 ± 0.064
0.750	0.100	0.51 ± 0.07	0.080 ± 0.016	0.041 ± 0.009	0.022 ± 0.005	0.0044 ± 0.0019	0.0055 ± 0.0019	-0.087 ± 0.071
0.900	0.200	0.50 ± 0.05	0.069 ± 0.011	0.028 ± 0.006	0.0155 ± 0.0031	0.0064 ± 0.0017	0.0034 ± 0.0011	-0.141 ± 0.064
1.100	0.200	0.30 ± 0.04	0.042 ± 0.008	0.018 ± 0.004	0.0041 ± 0.0016	0.0025 ± 0.0010	0.0013 ± 0.0007	-0.270 ± 0.080
1.300	0.200	0.16 ± 0.03	0.020 ± 0.006	0.005 ± 0.002	0.0023 ± 0.0012	0.0012 ± 0.0007	0.0003 ± 0.0003	-0.398 ± 0.128
$\frac{d\sigma}{dt}(t=0)$ from fit		100.3	49.8	30.9	19.51	12.88	9.61	
$\sigma_1(\mu b)=\int_{-1.5}^{0}\frac{d\sigma}{dt}\,dt$		22.6 ± 1.1	9.8 ± 0.5	5.61 ± 0.25	3.20 ± 0.14	2.02 ± 0.09	1.44 ± 0.06	
Number of Events		26,700	36,500	29,900	30,700	26,100	23,400	

Differential cross section in $\mu b/GeV^2$
for the charge exchange reaction.
α^* is the effective trajectory obtained
by fitting the fixed t data to a power law.

TABLE 5-1

used is shown, along with some of the corrected data, in figure 5-4. Table 5-2 gives the form of the empirical function used along with the results of fitting this form to the data. The largest correction was 30% and was dominated by the binning correction.

The data for the η and η' are shown in figures 5-5 through 5-8 and in tables 5-3 and 5-4.

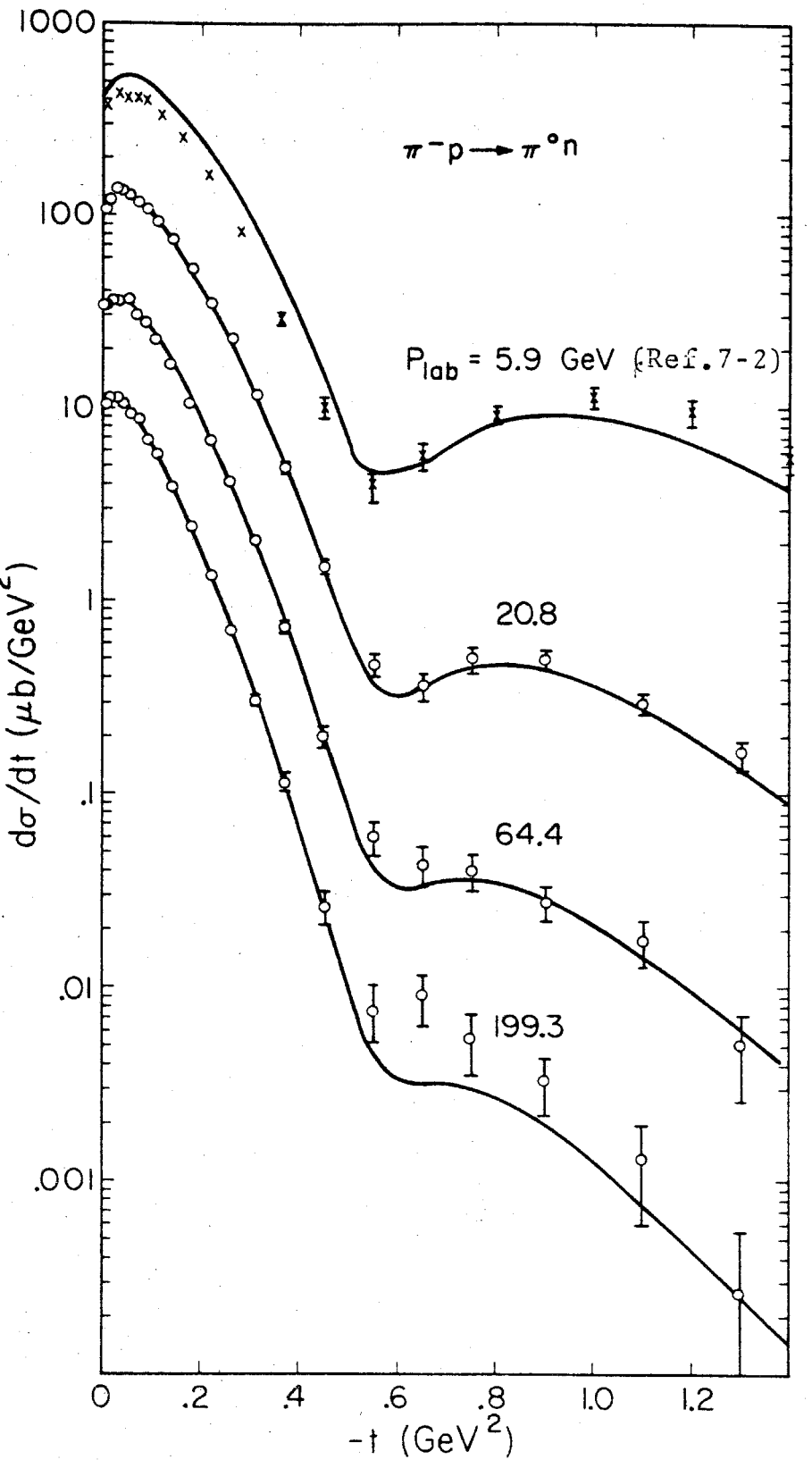
1000
100
10
1
.1
.01
.001
$d\sigma/dt$ ($\mu b/GeV^2$)
$\pi^- p \rightarrow \pi^\circ n$
P_{lab} = 5.9 GeV (Ref. 7-2)
20.8
64.4
199.3
0
.2
.4
.6
.8
1.0
1.2
$-t$ (GeV^2)

figure 5-4

TABLE 5-2

EMPERICAL FUNCTION USED TO FIT THE DATA

$$\frac{d\sigma}{dt} = \beta(t)\ \nu^{2\alpha(t)-2}$$

$$\nu = \frac{s-u}{4m_p} \simeq E_\pi + \frac{-t}{4m_p}$$

$$\beta(t) = \beta_1\ e^{b_1 t} - t(t-t_0)(\beta_2+\beta_3 t+\beta_4 t^2)e^{b_2 t}$$

$$\alpha(t) = \alpha_0+\alpha_1 t+\alpha_2 t^2$$

Results of fit

$\alpha_0 = 0.418 \pm 0.004$

$\alpha_1 = 0.928 \pm 0.034\ \text{GeV}^{-2}$

$\alpha_2 = 0.205 \pm 0.055\ \text{GeV}^{-4}$

$\beta_1 = 2340. \pm 80.$ nanobarns GeV^{-2}

$\beta_2 = (2.34 \pm 0.10)\times 10^5$ nanobarns GeV^{-8}

$\beta_3 = (-0.77 \pm 1.41)\times 10^5$ nanobarns GeV^{-10}

$\beta_4 = (11.6 \pm 5.4)\times 10^5$ nanobarns GeV^{-12}

$t_0 = -0.542 \pm 0.004\ \text{GeV}^2$

$b_1 = 5.20 \pm 0.21\ \text{GeV}^{-2}$

$b_2 = 6.16 \pm 0.61\ \text{GeV}^{-2}$

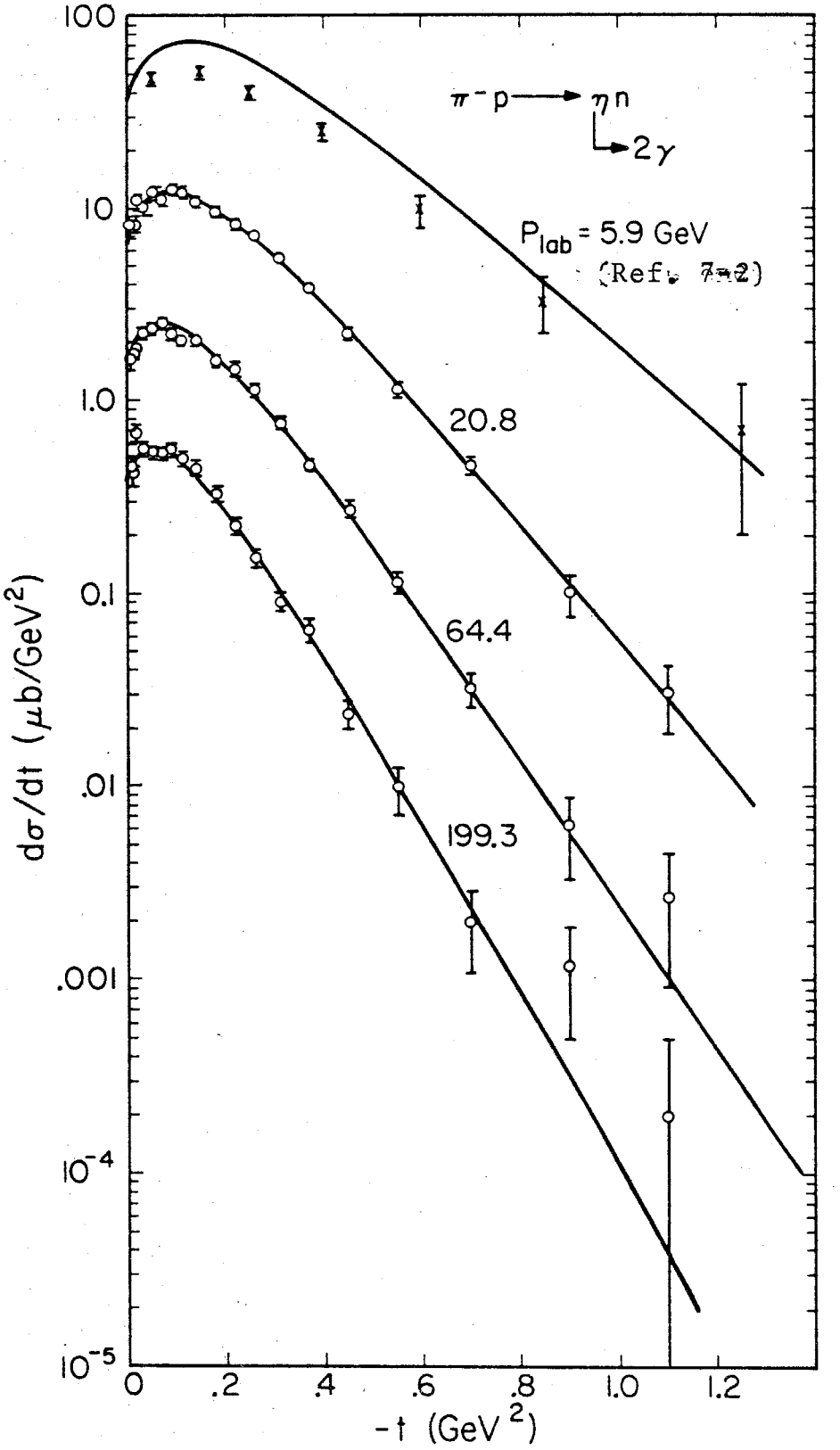
100
10
1.0
0.1
.01
.001
10^{-4}
10^{-5}
$d\sigma/dt$ (μb/GeV^2)
$\pi^- p \rightarrow \eta n$
$\hookrightarrow 2\gamma$
P_{lab} = 5.9 GeV
(Ref. 7-2)
20.8
64.4
199.3
0
.2
.4
.6
.8
1.0
1.2
-t (GeV^2)

figure 5-5

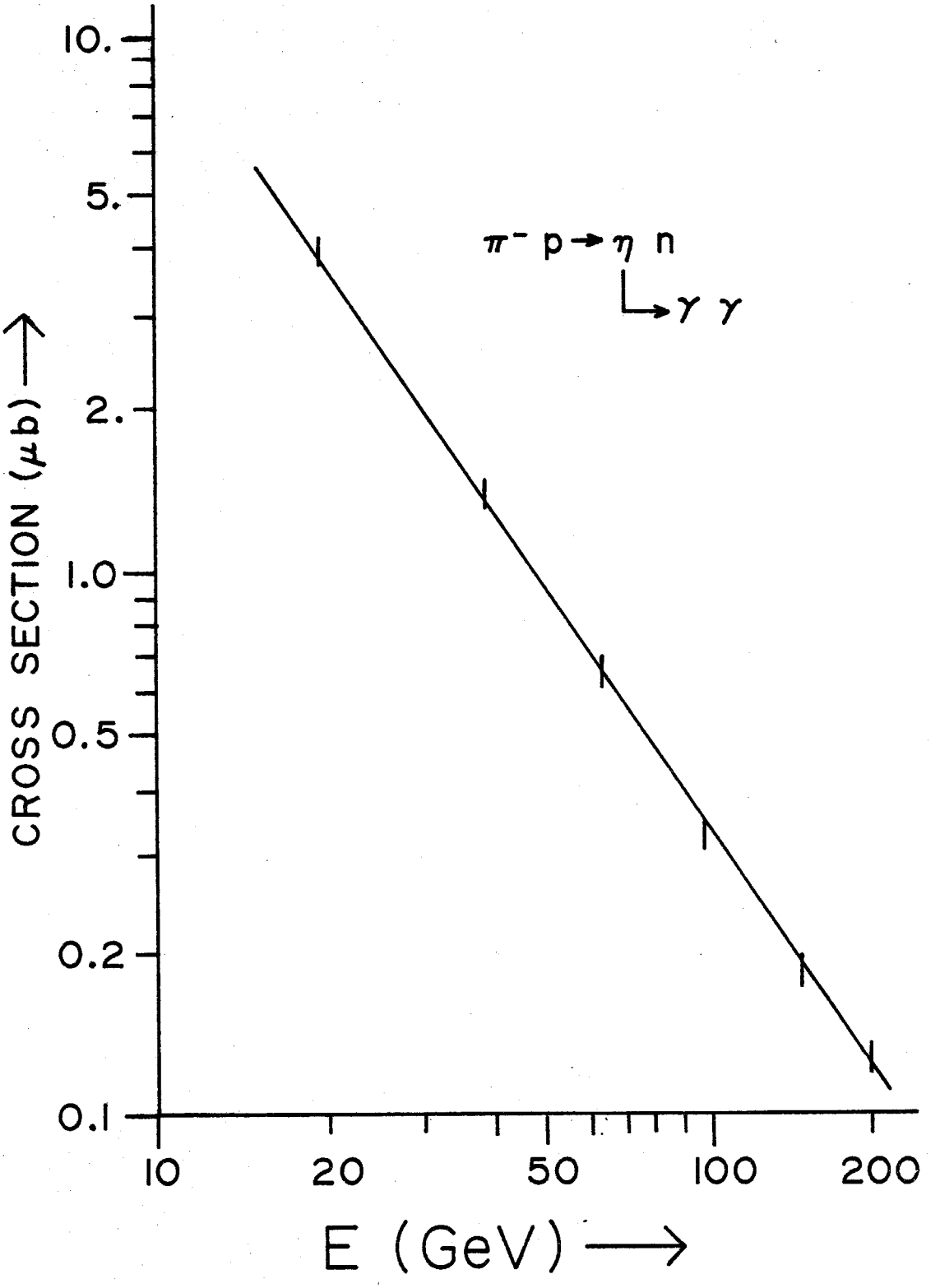

figure 5-6

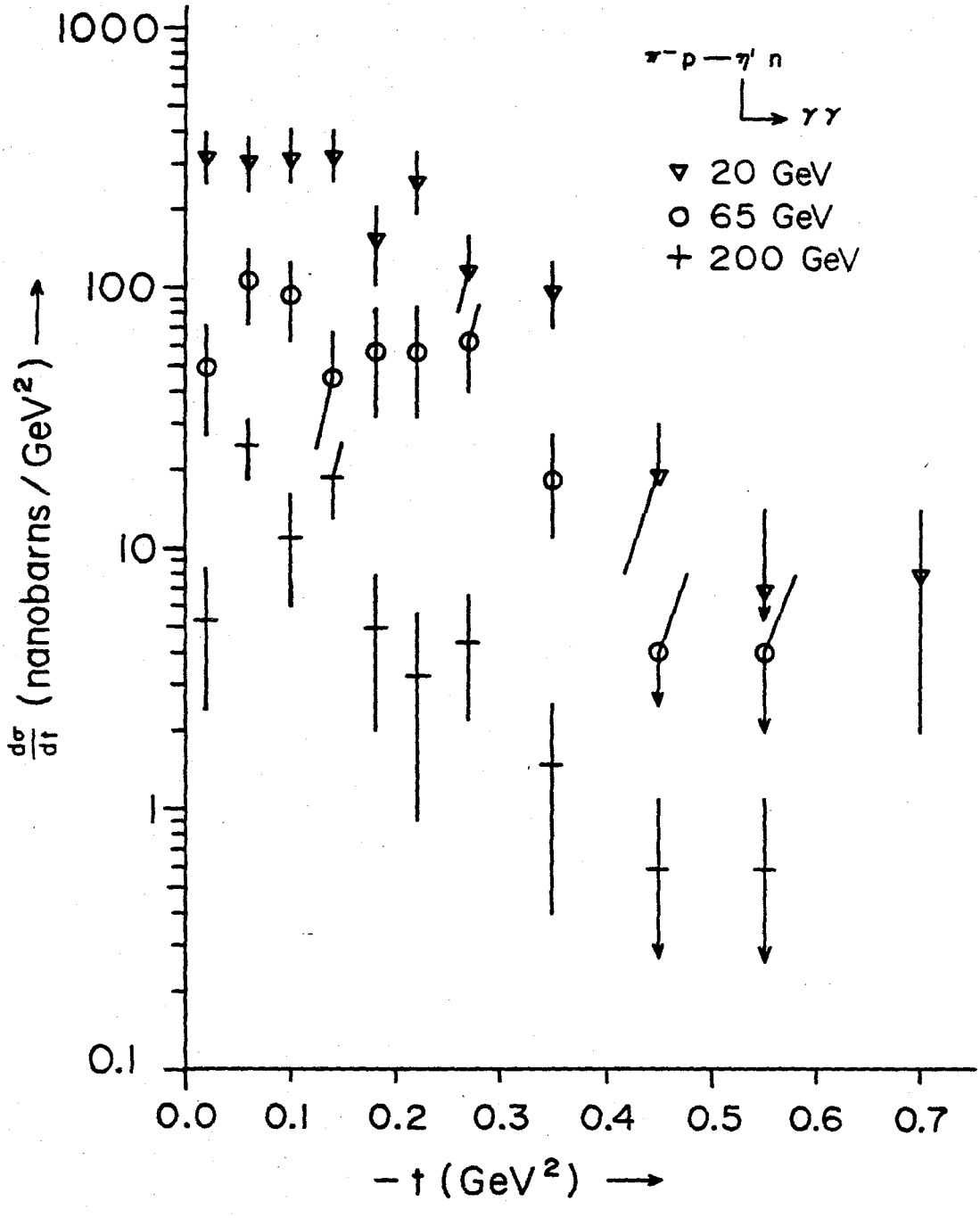
1000
100
10
1
0.1
$\frac{d\sigma}{dt}$ (nanobarns / GeV^2) ⟶
$\pi^- p \to \eta' n$
$\eta' \to \gamma\gamma$
20 GeV
65 GeV
200 GeV
0.0
0.1
0.2
0.3
0.4
0.5
0.6
0.7
$-t$ (GeV^2) ⟶

figure 5–7

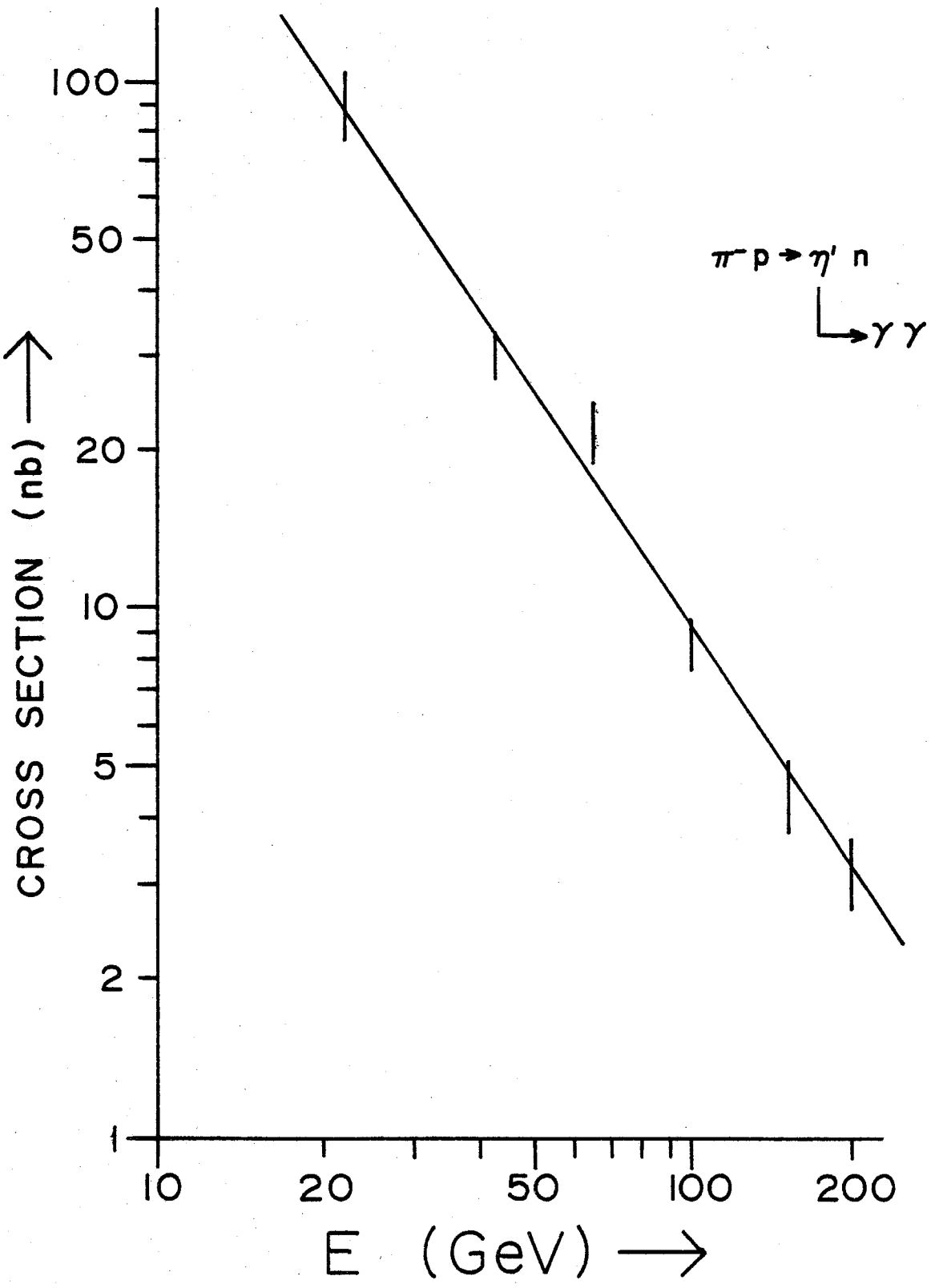
100
50
20
10
5
2
1
CROSS SECTION (nb) ⟶
$\pi^- p \to \eta' n$
$\eta' \to \gamma\gamma$
10
20
50
100
200
E (GeV) ⟶

figure 5-8

$-t$ (GeV^2)	Bin Width (GeV^2)	Beam Momentum in GeV						$\alpha^*(t)$
		20.8	40.8	64.4	100.7	150.2	199.3	
0.004	0.008	8.3 ± 1.0	3.14 ± 0.36	1.65 ± 0.20	0.98 ± 0.12	0.63 ± 0.08	0.46 ± 0.06	0.364 ± 0.036
0.012	0.008	8.5 ± 1.0	4.94 ± 0.46	1.82 ± 0.22	1.15 ± 0.14	0.74 ± 0.09	0.42 ± 0.06	0.333 ± 0.031
0.020	0.008	11.1 ± 1.2	3.87 ± 0.41	1.93 ± 0.23	1.41 ± 0.15	0.60 ± 0.08	0.69 ± 0.08	0.343 ± 0.034
0.032	0.016	10.2 ± 0.8	4.19 ± 0.31	2.24 ± 0.17	1.09 ± 0.09	0.84 ± 0.07	0.57 ± 0.05	0.355 ± 0.023
0.050	0.020	12.1 ± 0.8	4.52 ± 0.28	2.40 ± 0.16	1.31 ± 0.09	0.82 ± 0.06	0.55 ± 0.04	0.319 ± 0.019
0.070	0.020	11.0 ± 0.7	4.73 ± 0.28	2.56 ± 0.17	1.41 ± 0.09	0.82 ± 0.06	0.54 ± 0.04	0.335 ± 0.018
0.090	0.020	12.8 ± 0.8	4.70 ± 0.28	2.22 ± 0.16	1.42 ± 0.09	0.89 ± 0.06	0.56 ± 0.04	0.320 ± 0.019
0.110	0.020	12.3 ± 0.8	4.80 ± 0.29	2.09 ± 0.15	1.18 ± 0.09	0.61 ± 0.05	0.50 ± 0.04	0.261 ± 0.020
0.140	0.040	11.0 ± 0.5	4.22 ± 0.20	2.10 ± 0.11	1.08 ± 0.06	0.65 ± 0.04	0.447 ± 0.028	0.285 ± 0.015
0.180	0.040	9.9 ± 0.5	3.76 ± 0.18	1.68 ± 0.10	0.94 ± 0.06	0.423 ± 0.030	0.331 ± 0.024	0.226 ± 0.016
0.220	0.040	8.5 ± 0.5	2.99 ± 0.17	1.48 ± 0.09	0.73 ± 0.05	0.357 ± 0.028	0.229 ± 0.020	0.204 ± 0.017
0.260	0.040	7.4 ± 0.4	2.30 ± 0.14	1.15 ± 0.08	0.54 ± 0.04	0.236 ± 0.023	0.153 ± 0.016	0.147 ± 0.020
0.310	0.060	5.56 ± 0.32	1.84 ± 0.11	0.78 ± 0.06	0.344 ± 0.027	0.170 ± 0.016	0.091 ± 0.010	0.105 ± 0.019
0.370	0.060	3.91 ± 0.26	0.97 ± 0.07	0.47 ± 0.04	0.208 ± 0.021	0.105 ± 0.012	0.065 ± 0.009	0.094 ± 0.026
0.450	0.100	2.23 ± 0.15	0.64 ± 0.05	0.279 ± 0.025	0.109 ± 0.012	0.052 ± 0.007	0.024 ± 0.004	0.033 ± 0.025
0.550	0.100	1.16 ± 0.11	0.27 ± 0.03	0.117 ± 0.016	0.046 ± 0.008	0.0166 ± 0.0038	0.0100 ± 0.0028	-0.042 ± 0.039
0.700	0.200	0.47 ± 0.05	0.093 ± 0.013	0.033 ± 0.006	0.0134 ± 0.0031	0.0037 ± 0.0014	0.0020 ± 0.0009	-0.178 ± 0.053
0.900	0.200	0.102 ± 0.023	0.019 ± 0.006	0.006 ± 0.003	0.0034 ± 0.0016	0.0016 ± 0.0009	0.0012 ± 0.0007	-0.068 ± 0.128
1.100	0.200	0.031 ± 0.012	0.011 ± 0.004	0.0027 ± 0.0018	0.0015 ± 0.0010	0.0012 ± 0.0008	0.0002 ± 0.0003	-0.012 ± 0.156
$\frac{d\sigma}{dt}(t=0)$ from fit		6.71	2.88	1.62	0.92	0.558	0.391	
$\sigma_1(\mu b)=\int_{-1.5}^{0}\frac{d\sigma}{dt}\,dt$		3.85 ± 0.24	1.36 ± 0.09	0.647 ± 0.044	0.337 ± 0.021	0.184 ± 0.012	0.125 ± 0.008	
Number of events		4500	5100	3500	3300	2500	2100	

Differential cross section in $\mu b/GeV^2$
for the reaction $\pi^- + p \rightarrow \eta + n$.
α^* is the effective trajectory obtained
by fitting the fixed t data to a power law.

TABLE 5-3

η' Differential Cross Section Times Branching Ratio into $\gamma\gamma$ in Nanobarns/GeV^2

	20 GeV	40 Gev	65 GeV	100 GeV	150 GeV	200 GeV
0.00 - .04	324±74	77±22	49±22	16± 7	25.0±7.5	5.4±3.0
.04 - .08	307±72	152±32	107±32	46±11	16.0±6.0	25.0±6.7
.08 - .12	335±76	139±30	94±31	46±11	16.0±6.0	11.0±5.0
.12 - .16	335±76	111±28	46±23	35±11	16.0±6.0	19.0±6.0
.16 - .20	159±53	104±27	58±26	13± 6	16.0±6.0	5.0±3.0
.20 - .24	265±71	49±17	58±26	25± 9	13.0±5.7	3.3±2.4
.24 - .30	118±37	49±14	62±22	15± 6	6.8±3.4	4.4±2.2
.30 - .40	97±27	18± 7	19± 8	6± 3	1.8±1.3	1.5±1.1
.40 - .50	19±11	5± 4	4± 4	2± 2	1.8±1.3	.6± .6
.50 - .60	7± 7	0± 3	4± 4	0± 1	0.0±1.0	.6± .6
.60 - .80	8± 6	5± 3	0± 2	0±.5	0.0± .5	0.0± .4
.80 -1.00	7± 7	0±1.5	0± 2	0±.5	0.0± .5	0.0± .4
$\frac{d\sigma}{dt}\Big\|_{t=0}$						
$\sigma\int_{-1}^{0}\frac{d\sigma}{dt}dt$	91.0±8.0	31.0±2.9	23.0±3.1	9.1±1.0	4.7± .65	3.4± .5
Events	128	118	54	77	52	46

TABLE 5-4

6. The Multiphoton States

The analysis of the other final states was besieged by large backgrounds, low statistics and the limited acceptance of the apparatus. We successfully reconstructed more than 50% of the $\pi^0\pi^0$ and $\pi^0\eta$ events and saw strong f^0 and A_2 signals. The uncertainties in these final states involving particles with spin led to an inability to determine the spin density matrix elements. This in turn made it impossible to properly correct for the losses in the region where the acceptance was low.

6.1 The $\delta(980)$

The only spin zero particle to be observed in only the multiphoton states was the $\delta(980)$, which was observed through its decay into $\pi^0\eta$. Due to large backgrounds at the lower energies, the δ was only measured at the four highest energy settings. At these highest energies the number of events was only sufficient to make a rough determination of the integrated cross section. Figure 6-1 shows a characteristic $\pi^0\eta$ mass distribution while figure 6-2 shows the integrated cross section as a function of energy. Fitting these data to the power law aE^b, with E measured in GeV, yielded values for a and b of $4.9 \pm 2.$ microbarns and -1.20 ± 0.35, respectively.

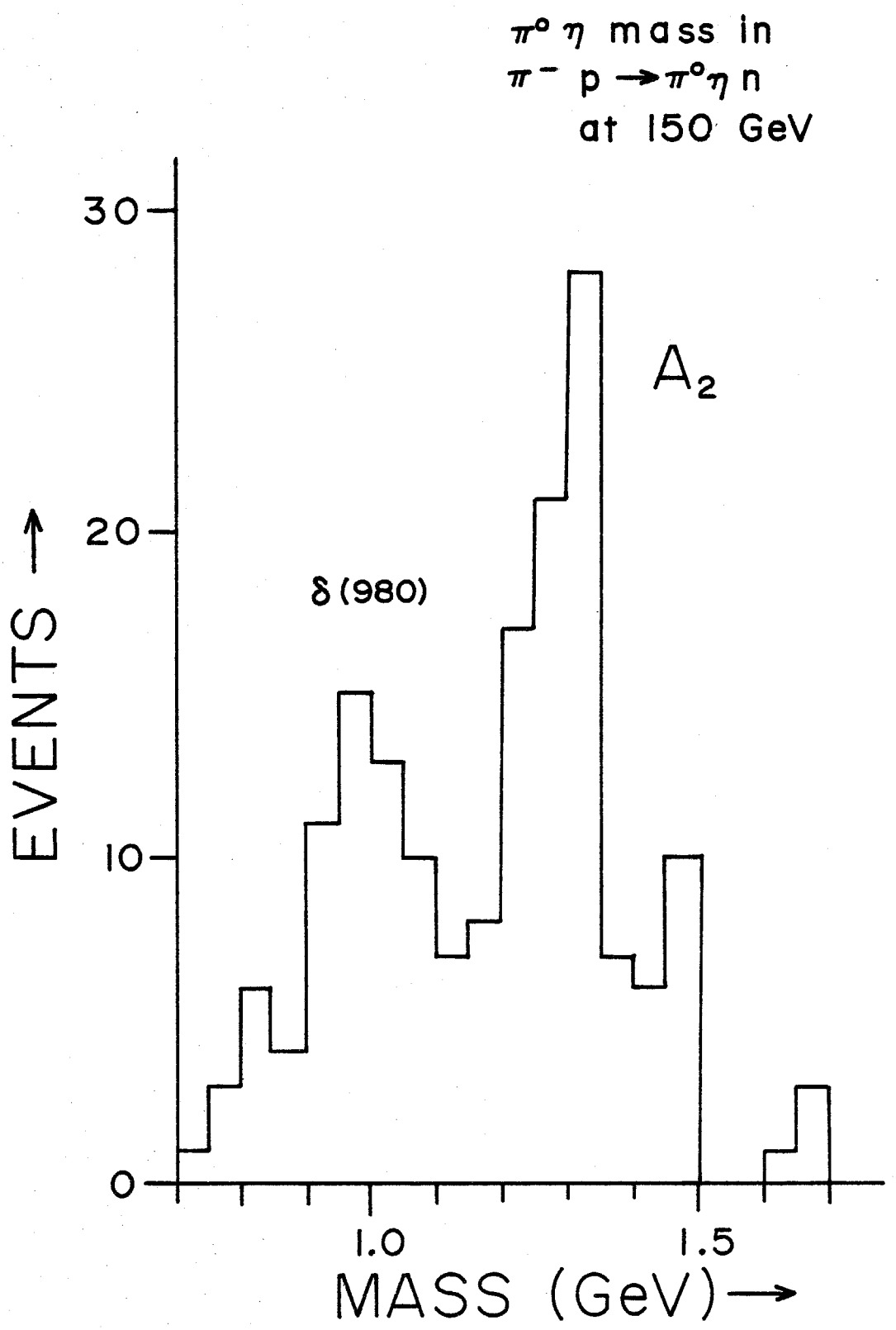
$\pi^0\eta$ mass in
$\pi^- p \rightarrow \pi^0\eta n$
at 150 GeV
30
20
10
0
EVENTS →
A_2
δ(980)
1.0
1.5
MASS (GeV) →

figure 6-1

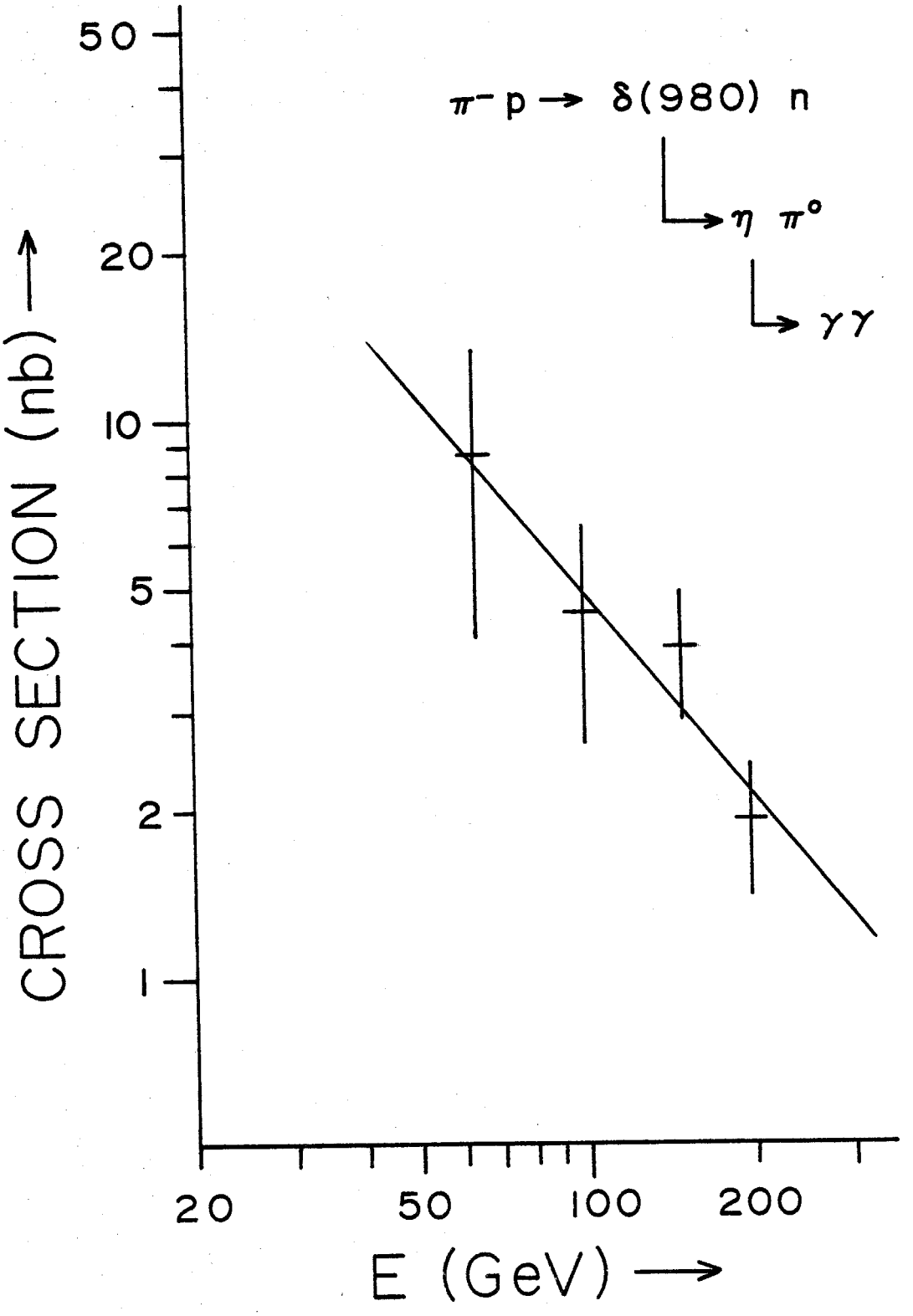

figure 6-2

The spin parity ($\emptyset^+$) and isospin (1) of the indicate that, from a Regge viewpoint, it can not be mediated by a ρ exchange, but that it is a pure B exchange process. If the slope of the B trajectory is similar to that for the other known particle families, the integrated cross section should fall more like $P^{-2.3}$. This is not completely ruled out by the data, but the confidence level for this hypothesis is only 1%. A few points at lower energies would help to clear this up.

6.2 Branching Ratio For $\eta \rightarrow \pi^\circ \gamma \gamma$

Measurements of the partial decay rate of the η into $\pi^\circ\gamma\gamma$ reported in the literature (reference 6-1, Particle Data Group) have been in contradiction with each other and all known theoretical calculations (reference 6-2) for several years. The decay rates for the pseudoscalar mesons can be calculated using a wide variety of phenomenological techniques. Virtually all of these calculated decay rates have been made to agree to within a factor of two with the measured rates except this one. The calculations for this decay predict a width of around 10^{-2} eV while the measured value is 28 eV. All these techniques at some stage use chiral invariance or weakly broken chiral invariance. It is not clear why these techniques should work for all the other decays and fail so completely for this one.

We looked for this decay mode in these data but found no sign of it. Events in the η mass region, selected by a cut on the mass as calculated from the moment method, were analyzed using the photon finding technique. Those which satisfied a four photon hypothesis were fitted to a $\pi^o\gamma\gamma$ interpretation. This same analysis was carried out on Monte Carlo generated events of two classes. The first class consisted of η decays into three π^o's while the second consisted of $\pi^o\pi^o$ events to simulate the nonresonant background under the η. The analysis of the $\pi^o\pi^o$ sample had almost no events which satisfied a $\pi^o\gamma\gamma$ hypothesis which did not also satisfy a $\pi^o\pi^o$ hypothesis. Some of the three π^o Monte Carlo events did fit the $\pi^o\gamma\gamma$ hypothesis without satisfying the $\pi^o\pi^o$ hypothesis. The chisquare, $\gamma\gamma$ mass and π^o mass distributions of the real data, satisfying the $\pi^o\gamma\gamma$ hypothesis and not also satisfying the $\pi^o\pi^o$ hypothesis, were indistinguishable from those distributions obtained from the η to three π^o Monte Carlo analysis. After subtracting the properly normalized three π^o background from the data, an upper limit on the branching ratio was determined to be

$$[\eta \rightarrow \pi^o\gamma\gamma]/[\eta \rightarrow \gamma\gamma] < 0.01 \quad (95\% \text{ CL}).$$

The current best value for this ratio from the Particle

Data Group is 0.082 ± 0.028. This number and the asscciated error are the result of a fit to all branching fractions using the measurements for all the known decay modes. The discrepancies in the past measurements of this ratio are so large and nonstatistical that the error they quote has very little meaning. Most of the previous measurements with a nonzero result made little or no allowance for contamination from the three π^o decays.

6.3 $\eta\pi\pi$ Decays And The $\eta' \rightarrow \gamma\gamma$ Decay Fraction

The η' has a decay into $\eta\pi^o\pi^o$ which was also observed in the data. All the events, with sufficient mass as determined by the moment technique, were analyzed using the photon finding method. Those with six photons found were fitted to an $\eta\pi^o\pi^o$ hypothesis with each of these decaying into two photons. A set of Monte Carlo generated η' events decaying in this mode were treated in the same way. A typical mass distribution of the data events is shown in figure 6-3.

The only clear signal in this decay mode is the η'. The limited acceptance of the apparatus excludes seeing $\eta\pi^o\pi^o$ decays in which the η and one of the π^o's resonate at a reasonably high mass or where the decay is highly polarized. With these limitations in mind, we can make the

π^- p — η' n
with the η' decaying
into $\eta\ \pi^\circ\ \pi^\circ$
at 100 GeV

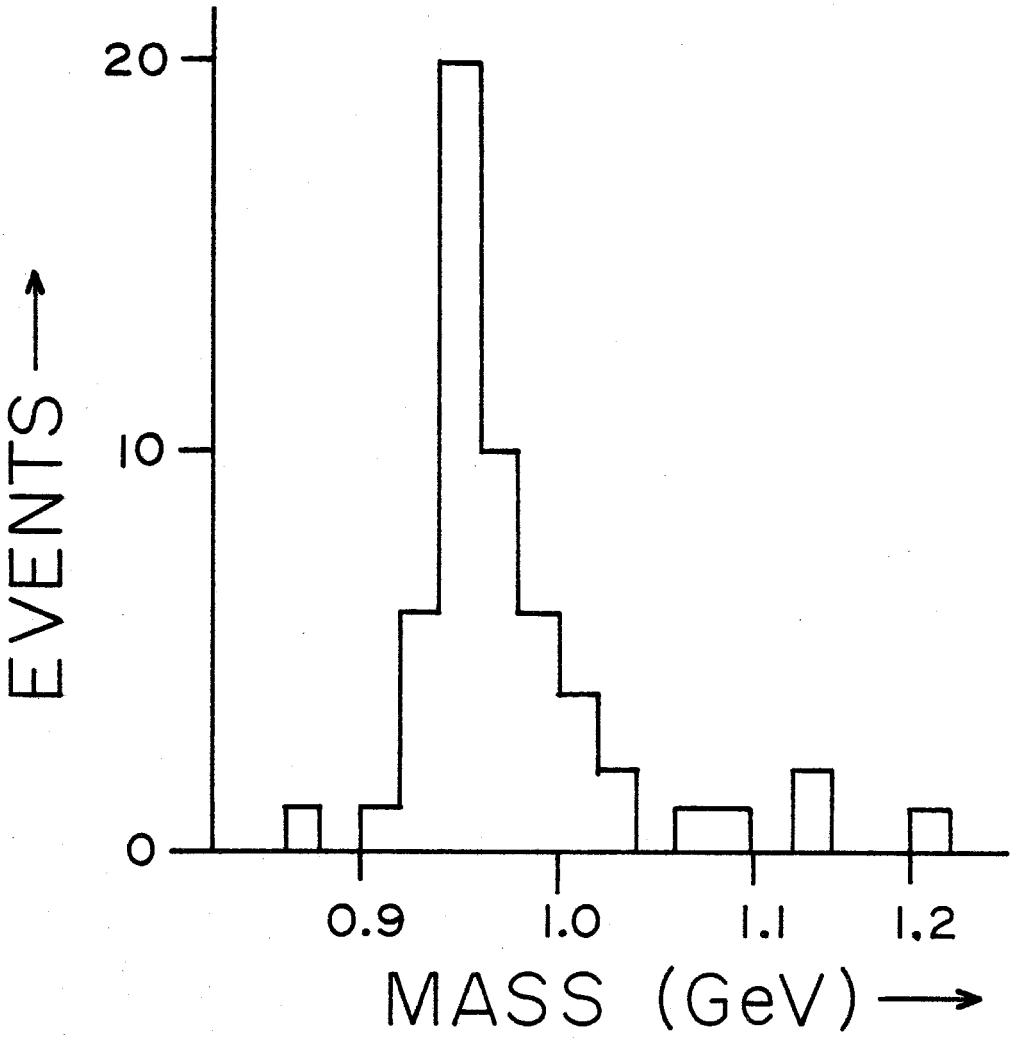

figure 6–3

weak statement that any unpolarized high mass particles decaying into $\eta\pi^\circ\pi^\circ$ with nonresonant $\eta\pi^\circ$ will have a cross section times branching ratio which is less than 10% of that for the η'.

A crude determination of the branching ratio of

$$[\eta' \to \gamma\gamma]/[\eta' \to \eta\pi^\circ\pi^\circ]$$

with the η subsequently decaying into two photons, was also made. The branching ratio is about 0.20 ± 0.04, where the error is purely statistical. There is a serious systematic error coming from the Monte Carlo determination of the program efficiency. When the analysis was performed with different values of the parameters used in the photon finding, the efficiency for finding the η' to $\eta\pi^\circ\pi^\circ$ decay varied rapidly. These variations were due to the change in the efficiency of finding very low energy photons. Since the distribution of photon energies in this decay mode is peaked at low energies, this effect is very important. The spatial distribution of energy in the detector from these low energy photons is very irregular. Even though the Monte Carlo cannot reproduce these irregularities, tests indicate that the efficiencies from the Monte Carlo are probably good to better than 30%. Using this as the systematic uncertainty gives a branching ratio of

$$[\eta' \to \gamma\gamma]/[\eta' \to \eta\pi^0\pi^0] = 0.20 \pm 0.06,$$

where the $\eta\pi^0\pi^0$ decays to six photons.

7. Conclusions

The pion-nucleon charge exchange data have been analyzed in several ways to compare them with different phenomenological ideas. These data, spanning the laboratory energies from 20 to 200 GeV, momentum transfers from 0.0 to -1.2 GeV^2 and five orders of magnitude in differential cross section, represent the best kinematic region yet measured for the application and study of the Regge idea. They also extend the region over which the forward scattering amplitudes may be over determined. When taken along with the total cross sections and the very small angle elastic scattering differential cross sections, they may be used to test the consistency of the existing data with the forward dispersion relations.

7.1 Regge Behavior

In its simplest form, the Regge pole model predicts that the differential cross sections at fixed momentum transfer, t, vary with the beam energy as a power of that energy. We fitted our differential cross sections at fixed t to such a form and extracted an effective Regge trajectory. The values for the trajectory obtained are shown in figure 7-1 along with the curve obtained from the fit described in chapter 5. These data taken alone are

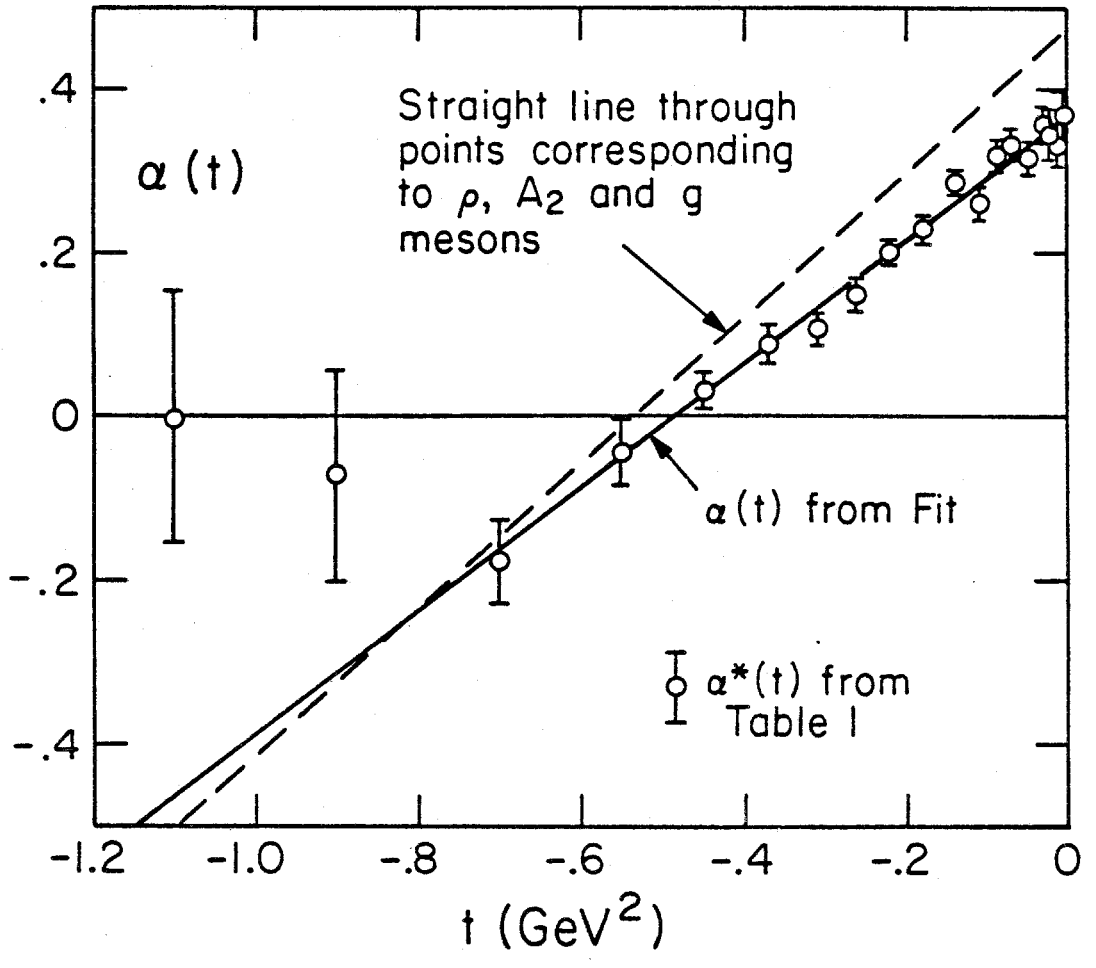

Effective rho meson Regge trajectory extracted from the differential cross section measured for the reaction

$\pi^0 + p \rightarrow \pi^- + n$

Figure 7-1

completely consistent with this naive Regge pole model.

The data sets at the different energies have also been fitted to determine the t dependence at fixed energy. Each set was fitted to the empirical function described in chapter 5 with the trajectory function, $\alpha(t)$, fixed at the value determined by the fit described in that chapter and the residue function, $\beta(t)$, allowed to vary. In general, the parameters obtained for the function β were changed only slightly from their values obtained from the fit to the data sets from all energies taken together. In particular, the parameter t_o, which is a measure of the position of the dip in the differential cross section, varied only slightly. The values of t_o obtained for the different energies are presented in figure 7-2 along with the positions of the dips extracted from some of the lower energy data by fitting them to this parameterization. In comparing the dip positions at different energies and for different experiments, one should realize that the t scales used may be systematically different. For our data we expect the energy to energy t scale to vary by about 2%. It is difficult to extract the t scale uncertainties for other experiments. Notice, however, that the apparent discrepancy between the 40 GeV Serpukhov data(reference 7-1) and our 40 GeV point vanishes if their t scale is assumed to differ from ours by only 4%.

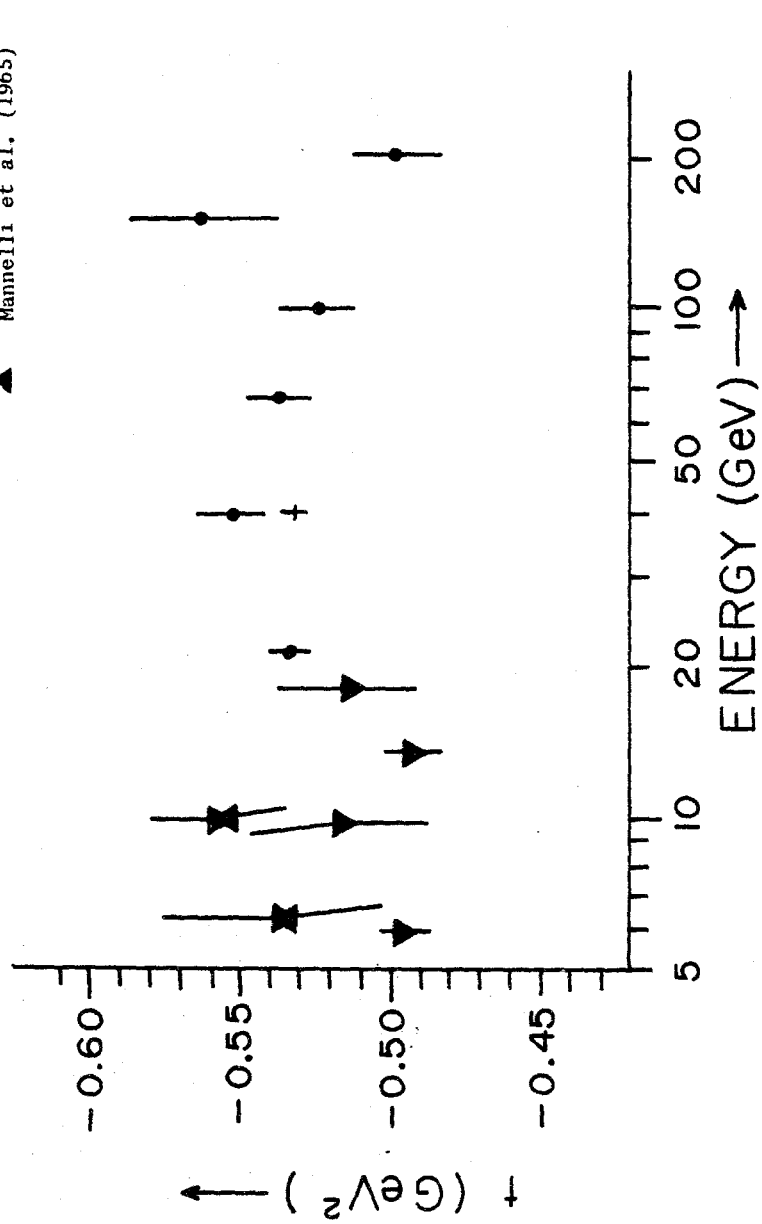

figure 7-2

Position of the dip in the charge exchange differential cross section. See text for a description of the unfolding proceedure

At the higher energies one might have expected to observe a breakdown of this simple model, which was based on the exchange of a single Regge trajectory. One expects, and to satisfy unitarity needs, other structures in the complex angular momentum plane such as cuts, fixed poles and branch points. When the lower energy data (reference 7-2) and the polarization data (reference 7-3) are taken into account, there are deviations from the naive model. However, these deviations are not large enough to conclusively distinguish between various phenomenologically expected sources of deviation. Barger and Phillips (reference 7-4) supplement the naive model with a second exchange trajectory and are able to account for the deviations observed. Others invoke cuts (reference 7-5) which come from simultaneous exchanges of both the ρ and pomeron trajectories. All these Regge schemes can fit the existing data well.

7-2 Relation To Total Cross Section Differences

Using isospin invariance and the optical theorem, the charge exchange differential cross section in the forward direction can be related to the total pion-nucleon cross sections. In chapter 1 it was pointed out that the charge exchange amplitude could be related to the elastic scattering amplitudes through isospin invariance. The total cross section can be related to the imaginary part of the

forward elastic scattering amplitude through the optical theorem. Specifically in units with h=c=1,

$$\sigma = \frac{4\pi}{P} \mathrm{Im}(A(0))$$

where P is the center of mass momentum
σ is the total cross section
and $A(\emptyset)$ is the amplitude for elastic scattering in the forward direction.

Combining this with the isospin relation between elastic scattering and charge exchange and defining $\Delta\sigma$ to be the difference between the $\pi^+ p$ and $\pi^- p$ total cross sections, yields the relationship

$$\mathrm{Im}(A_{CEX}(\emptyset)) = P\,\Delta\sigma / [4\pi\sqrt{2}].$$

Furthermore, if the ratio of the real to imaginary parts of the forward scattering amplitude is taken to be R, then, after converting to units where the differential cross section is in microbarns and the total cross section difference is in millibarns, the charge exchange differential cross section in the forward direction is related to the cross section difference by

$$\frac{d\sigma}{dt} = 25.54\,(R^2+1)(\Delta\sigma)^2$$

This relationship can be used either to measure R or, if R can be obtained in another way, to compare the experimental measurements. If the simple Regge behavior persists at much higher energies, we can use dispersion relationships to get R in terms of the trajectory function evaluated at t=Ø, $\alpha(0)$. The result is $R=\tan[\pi\,\alpha(0)/2]$. This relationship holds fairly well as can be seen from figure 7-3 where the total cross section differences are plotted along with the prediction from charge exchange. The extrapolation to t=Ø and the value of $\alpha(0)$ are from the fit in chapter 5.

Engelmann and Hendrick (reference 7-6) have made a dispersion relationship analysis of all the total cross section data to extract the real parts of the amplitudes. Their results do not agree with our data for the ratio R. This disagreement is rather small and may be due to one of many effects. In their fits they include data for the $\pi^- p$ total cross section from both the Serpukhov experiment (reference 7-7) and the Fermilab experiment (reference 7-8). These two experiments disagree with one another far more than the ratio R from their work disagrees with the value inferred from our data. Although they varied the way they extrapolated the cross sections to infinite energies, they did not consider the possibility that the cross section for $\pi^+ p$ and $\pi^- p$ might have slightly different structures at

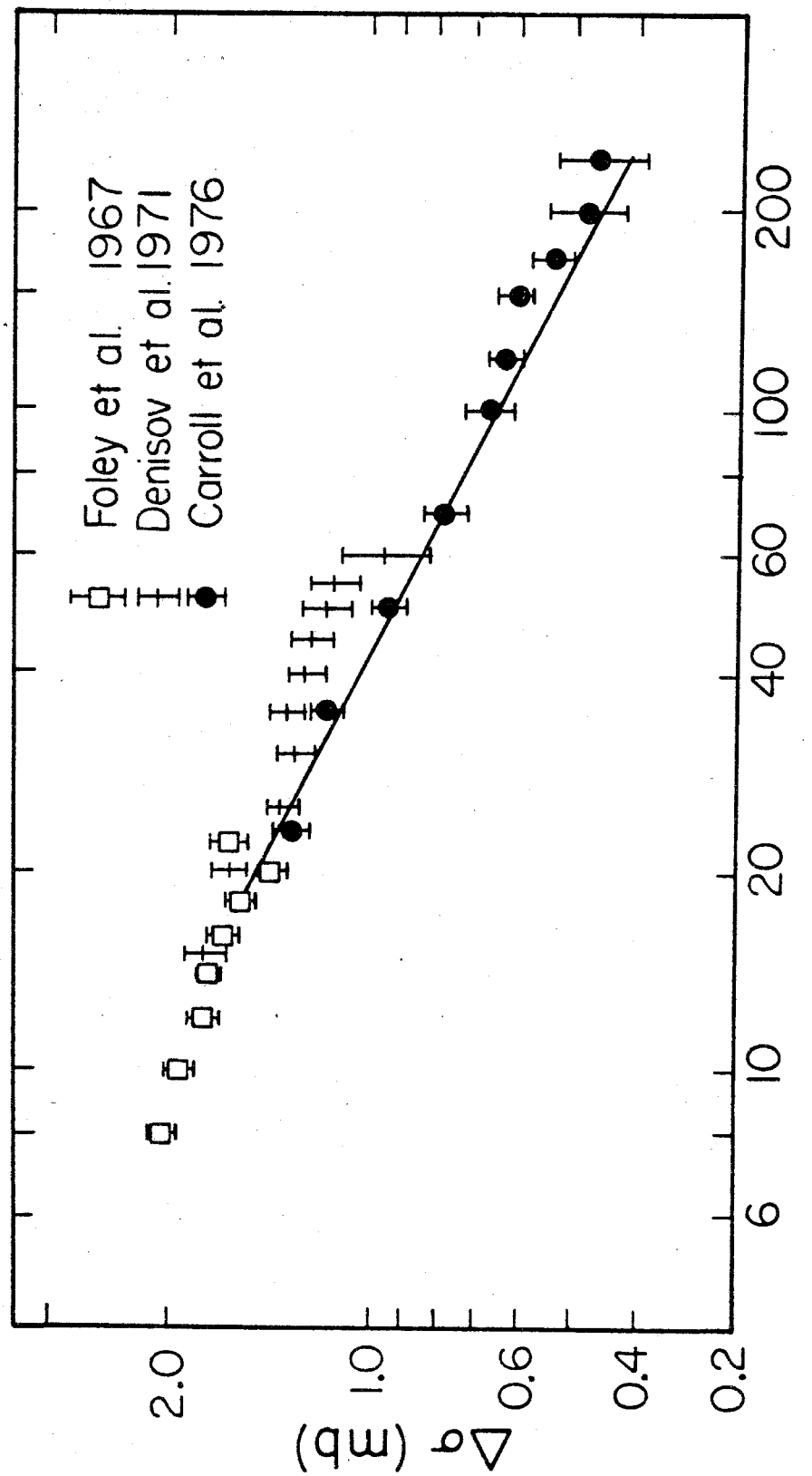

figure 7-3

Total cross section difference between π^+ and π^- scattering from protons along with the prediction from the forward charge exchange cross section.

energies just above 200 GeV. This kind of behavior is unlikely in light of the continuing fall off of the forward charge exchange cross section, but even very small deviations would be capable of bringing the values for R into agreement. Analyses such as theirs are interesting in that the input assumptions made are very fundamental. An extension of their analysis to take into account the recent elastic scattering data as well as our data on charge exchange would provide an interesting test of these very fundamental ideas.

7.3 The η,η' Mixing

In an SU(3) quark model the states made of two quarks are naturally represented by an octet and a singlet. The singlet always has the same quantum numbers as one of the members of the octet. These states can and do mix to produce two physical particles. In the $\mathcal{C}^-$ octet the particles which are a mixture of the singlet and octet states are the η and the η'. The $\mathcal{C}^-$ singlet and octet states can be written as linear combinations of the quark antiquark states as follows:

$$\eta_8 = (1/\sqrt{6})[u\bar{u}+d\bar{d}-2s\bar{s}]$$
$$\eta_1 = (1/\sqrt{3})[u\bar{u}+d\bar{d}+s\bar{s}]$$

where η_8 is the octet state

η_1 is the singlet state

and $u\bar{u}$, $d\bar{d}$ and $s\bar{s}$ are the quark states.

And the physical particles are in turn linear combinations of these two states as

$$\eta = \cos(\theta)\eta_8 - \sin(\theta)\eta_1$$
$$\eta' = \sin(\theta)\eta_8 + \cos(\theta)\eta_1$$

where θ is the mixing angle.

If one assumes the above quark model representation of these particles and assumes the quark line rule (also known as Zweig's Rule) one is led to the conclusion that in reactions of the form

$$\pi^- p \rightarrow X\, n$$

the unknown particle X must contain some $d\bar{d}$. Using these assumptions one concludes that the ratio of the cross sections for η and η' production should be a measure of the relative amounts of dd in the two physical states.

This measurement gives a cross section ratio of 0.5 ± 0.1. Using this alone gives a mixing angle of $\pi/2$. That would indicate that the η' is the purely octet and the η is purely singlet. This is not in agreement with two other pieces of information. First there are the mass relationship within the octet. These rules were the first success of the SU(3) ideas. They indicate that the mixing

angle should be either $\pm 11^{\circ}$ or $\pm 24^{\circ}$ depending on whether you prefer the linear or quadratic mass relationship. Second there are the electromagnetic properties of the particles. The radiative decay widths of the η have been measured and they agree well with the mixing angle of -11°. The calculated rate disagrees with the measurement by a factor of 8 if the mixing angle is taken to be $\pi/2$.

There seems to be something very wrong with the assumptions leading to the mixing angle of $\pi/2$. One explanation is that the quark line rule fails for the 0^- states do to two gluon couplings. However invoking the gluons lifts the lid from a box of horrors. The η, η' system may actually contain a component of two gluon states. In that case the η and η' could be very complicated mixtures of η_8, η_1 and glue. In that case there are many more mixing angles. Fortunately the measurements of the radiative decays of the particles are only consistent with the data if two gluon component is small. There is hope that this will be easy to resolve.

Finally there is the problem of charm and other flavors of quarks. If this glue effect is the cause of the break down of the quark line rule, why arn't the higher mass flavors of quarks mixed in with the η, η' system? This system seems to be too light to allow very much mixing with

the higher mass flavors.

Appendix 1. The Moment Method

The first three spatial moments of the energy distribution in the detector can be used to determine the energy, effective position and effective mass for any number of photons in the detector.

The energy is determined from the zeroth spatial moment using the formula below:

$$E = a\left(E_x + E_y\right)$$

$$E_x = \sum_{i=1}^{70} Phx_i \qquad (A1\text{-}1)$$

$$E_y = \sum_{i=1}^{70} Phy_i$$

where a is a proportionality constant relating pulse height units to energy units,

Phx_i is the pulse height in the i^{th} counter in the x view.

and Phy_i is the pulse height in the i^{th} counter in the y view.

The effective position of the photons is gotten directly as the first moment of the distribution as in the following formula for the x position:

$$\langle x \rangle = \sum_{i=1}^{70} x_i \, Phx_i \Big/ E_x \qquad (A1\text{-}2)$$

where x_i is the position of the center of the i^{th} counter in the x view.

The mass is computed from the first and second moments of the distribution from the following:

$$m^2 = \frac{E^2}{L^2}\left(x_{rms}^2 + y_{rms}^2 - 2\delta^2\right)$$

$$x_{rms}^2 = \langle x^2 \rangle - \langle x \rangle^2 \qquad (A1\text{-}3)$$

$$\langle x^2 \rangle = \sum_{i=1}^{70} x_i^2 \, Phx_i \Big/ E_x$$

where m is the mass of the decaying meson.

E is its energy,

L is the distance from the detector to the decay vertex,

and δ is the width of a single photon shower (approximately constant).

The first of these formulas is just a statement of the fact that the detector response is linear with energy. The second isn't so obvious, it is based on the linearity and the fact that the individual photon showers are symmetrical about their center. To study these formulas in further detail it is useful to think in terms of the energy deposited in each of the counters by each of the many photons. For example the first spatial moment of equation A1-2 becomes:

$$\langle x \rangle = \sum_{i=1}^{70} \sum_{j=1}^{n} x_i \, Phx_{ij} \Big/ E_x$$

where Phx_{ij} is the contribution of the j^{th} photon to the pulse height in the

i^{th} counter,

and n is the number of photons.

The inner sum is related to the single photon position

$$\langle x_j \rangle = \sum_{i=1}^{70} x_i \, Phx_{ij} \Big/ Ex_j$$

$$Ex_j = \sum_{i=1}^{70} Phx_{ij}$$

where $\langle x_j \rangle$ is the position of the j photon

and Ex_j is its energy.

Making this substitution yields

$$\langle x \rangle = \sum_{j=1}^{n} Ex_j \langle x_j \rangle \Big/ Ex$$

which only involves the parameters of the photons.

Momentum conservation arguments can easily be cast in forms containing the kinematic parameters of the decay. Project the meson direction onto the face of the detector to get the coordinates x and y where the meson would have hit. The momenta of the photons transverse to the meson direction must be zero as long as all the decay products are photons and are detected. The x component of this momentum is

related to the photon energies and angles by:

$$P_x = \sum_{j=1}^{n} E_j \sin \theta x_j$$

where θx_j is the x projection of the angle between the j^{th} photon and the direction of the meson.

For these experiments the angles are always less than a tenth of a radian allowing the use of the small angle approximation without any noticeable loss of precision. Therefore use

$$\theta x_j \simeq \frac{x_j - x_o}{L}$$

where x_j is the x-coordinate of the j^{th} photon,

x_o is the x-coordinate of the meson,

and L is the distance from the decay vertex to the detector.

With this substitution the x component of the transverse momentum becomes:

$$P_x = \sum_{j=1}^{n} \frac{E_j (x_j - x_o)}{L}$$

Since this component of the momentum must be zero this implies equation A1-2 namely:

$$\langle X \rangle = X_o = \sum_{j=1}^{n} E_j x_j \Big/ \sum_{j} E_j$$

The analysis of the second moment proceeds along the lines of that for the first moment. With the decomposition of equation A1-3 into terms involving only the individual photon parameters it becomes:

$$\langle x^2 \rangle = \sum_{j} Ex_j \langle x_j^2 \rangle \Big/ Ex$$

where

$$\langle x_j^2 \rangle = \sum_{i=1}^{70} x_i^2 \, Phx_{ij} \Big/ Ex_j$$

Since the RMS widths of the individual photons is almost

constant from photon to photon, it is convenient to rewrite this as:

$$\langle \chi^2 \rangle = \delta^2 + \sum_j E x_j \langle x_j \rangle^2 \Big/ E x$$

where δ is the individual photon width. Using this in equation A1-3 yields:

$$\chi^2_{rms} = \delta^2 + \sum_j E x_j \left(\langle x_j \rangle - \langle x \rangle \right)^2 \Big/ E x$$

Which contains only the photon energies and positions.

As with the first moment analysis a conservation principle is needed. Here the appropriate quantity is the energy minus the longitudinal momentum. Before the decay this quantity is:

$$E - P_{\parallel} = E - \sqrt{E^2 - m^2} \simeq \frac{m^2}{2E}$$

where E is the energy of the meson,

and m is its mass.

After the decay the same quantity for the photons is:

$$E - P_{11} = \sum_j E_j - P_j \cos\theta_j$$

where E_j is the energy of the j^{th} photon,

P_j is the magnitude of its momentum

and θ_j is the angle between it and the meson.

Equating these, using small angle approximations and using the fact that a photon's energy is equivalent to its momentum yields the desired equation A1-3.

Appendix 2. Photon Counting

A simple, reasonably efficient, technique for finding the positions and energies of the photons was required in order to separate those states having several photons. This problem looks straightforward since it is obvious "by eye" (as in figure A2-1) how many photons are present, where they are and how big they are. However, the combinations of possibilities when several photons are present (as in figure A2-2) makes the general algorithm difficult. The photon finding used in this analysis was rather naive, fairly fast and worked on a large fraction of the events.

First each counter in which the pulse height was greater than that in the adjacent counters, was tagged as a peak, and those in which the pulse height was lower than adjacent counters were tagged as valleys. Those peaks which were greater than at least one of the adjacent valleys by an amount corresponding to at least 0.5 GeV were considered as photon candidates.

Estimates of the position and energy of a candidate were made using the pulse heights in the peak counter and the two counters adjacent to it. Specifically, the difference between the pulse heights in the adjacent counters was divided by the pulse height in the peak

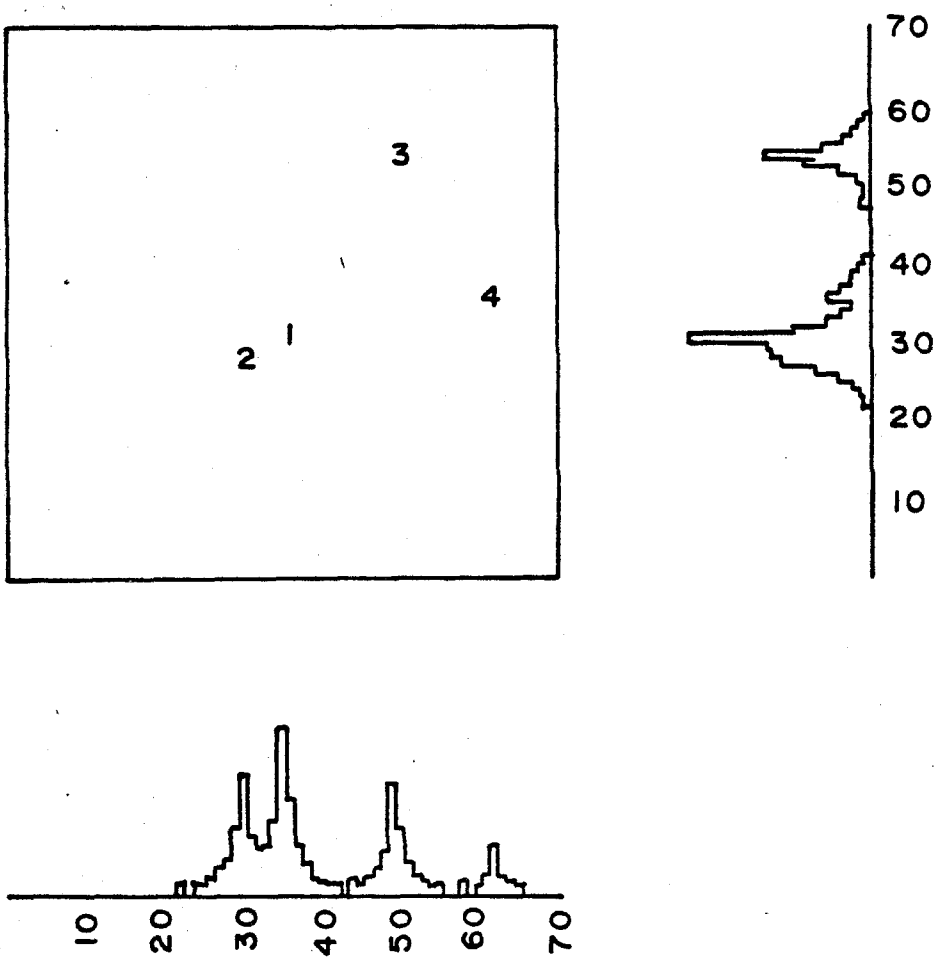
3
4
1
2
70
60
50
40
30
20
10
10
20
30
40
50
60
70
65 GeV $\pi^0\pi^0$ EVENT
MASS = 0.853 GeV

figure A2-1

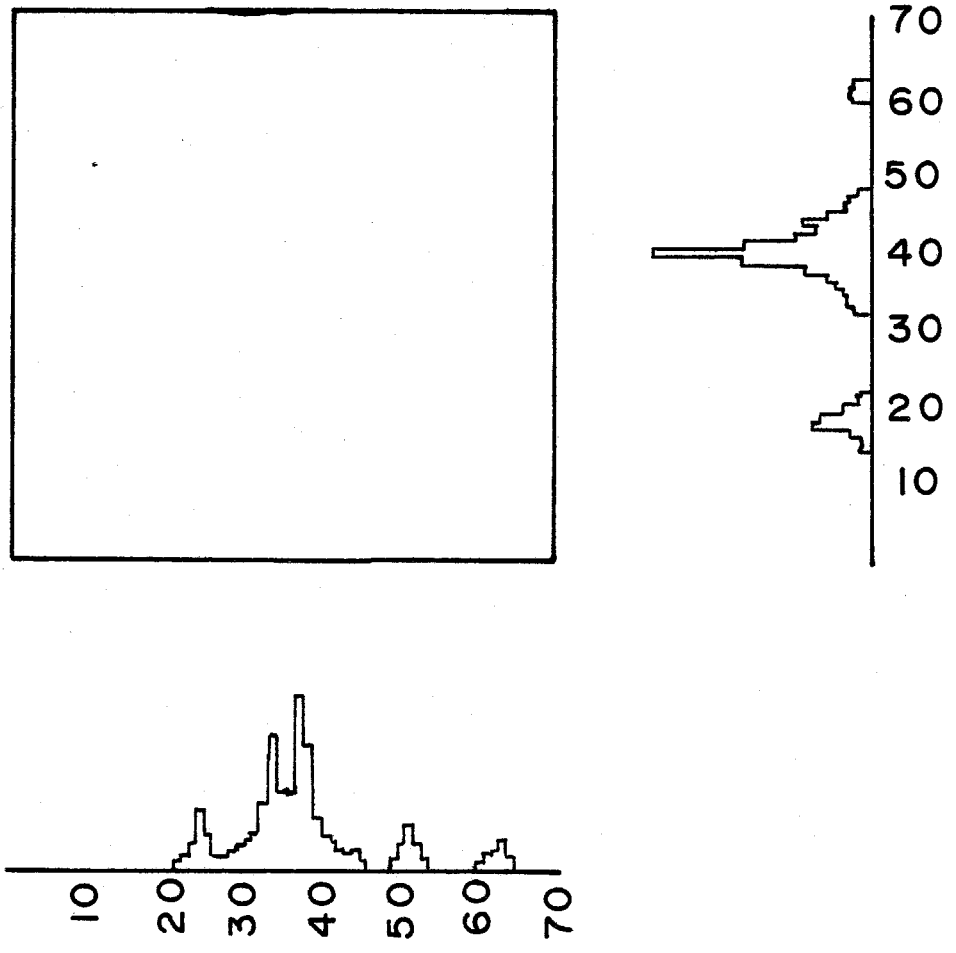

PROBABLY
$\eta \rightarrow 3\pi^{\circ}$
65 GeV

figure A2-2

counter. This quantity is monotonically related to the position of the peak by the empirically determined function shown in figure A2-3. The sum of the pulse heights in the three counters was multiplied by a factor of approximately 1.2 to give an estimate of the total pulse height of the photon shower. The precise factor depends on the value of the position but varies by less then 2% over the range of mu.

After this initial determination of photon positions and energies, several things were done to improve the quality of the pattern recognition. Each photon with an energy less than 6 GeV was examined and rejected if it was consistent with a fluctuation in the tail of a nearby large photon. If two photons were so closely spaced that the method of using the central three counters was not good enough, the pulse height data in those counters affected by the photons were reanalyzed by comparing them to empirically determined pulse heights and varying the positions and energies of the photons to give a best fit to the measured pulse heights. In some events the real photons overlapped, resulting in the initial determination treating them as a single photon. Some of those cases were recognized by noting that the two adjacent counters had more pulse height than expected from a single photon of that energy. These double photons were tagged and the energy of the pair was

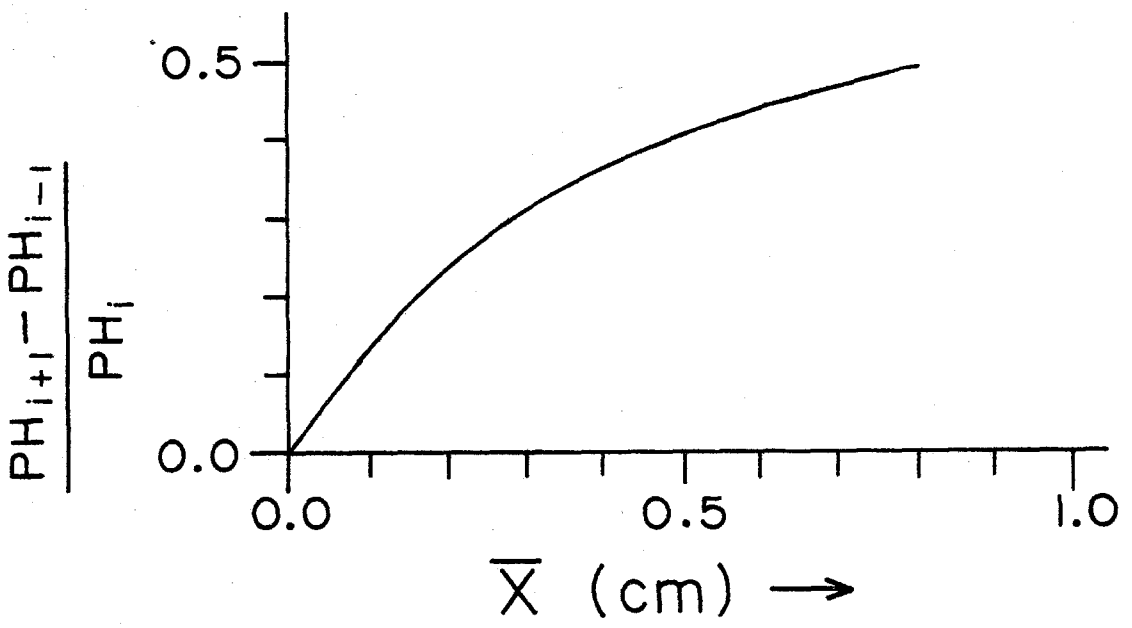

Emperical function relating the pulse heights in the three counters around the shower to the shower centroid.

figure A2-3

determined by summing the pulse heights over several counters.

Up to this point the data from the two views were analyzed separately. Each event was then assigned a photon count equal to the maximum of the peak counts in the two views. This scheme correctly classified the two photon events but was rather poor for events with low mass and many photons.

Many schemes were developed for treating the data from both views. Although some of these could untangle some very complicated events, they often got confused. The biggest problem was the rejection of the three π^o decay mode of the η. In a Monte Carlo study of 10^4 η events decaying in the three π^o mode, 8% were identified as being good four peak events in both planes while 9% were identified as having four peaks in one plane and less than four in the other. While these may seem to be modest fractions of the η decays, the η production cross section is so large that these misidentified η decays dominate the four photon signal.

Since the complicated schemes got so confused by these events, the following simple scheme was used: those events with the same peak count in each of the views were only fit to hypotheses with that photon count; those with a

difference of one in the peak count between the views were fit either to hypotheses with the higher number of photons or, if the smallest photon in the view with the greater count was consistent with a fluctuation in the tail of one of the other photons in the view, fit to hypotheses with the lower count; those events with a peak count difference of two or more between the planes were not included in the multiphoton analysis.

Appendix 3. The t Resolution

In the energy and momentum transfer region covered by this experiment the momentum transfer is very well approximated by

$$t = E^2 \theta^2$$

where E is the energy of the beam particle,
t is the momentum transfer
and θ is the laboratory scattering angle.

In this analysis t was calculated from the measured quantities according to the following formula:

$$t = \frac{E^2}{L^2} \left\{ (x_\pi - x_m)^2 + (y_\pi - y_m)^2 \right\}$$

where L is the distance from the target to the detector,
x_π is the x-coordinate of the incident beam particle projected onto the face of the detector,
x_m is the measured x-coordinate of the final state meson at the detector.
and y_π, y_m are the analogous quantities for the y-coordinate.

Each of the quantities in the above formula have associated with them uncertainties which can be represented by distribution functions. The variables E and L are particularly simple, each being approximately flatly distributed from a minimum to a maximum value. The coordinate variables, on the other hand, are considerably more complicated.

A naive first order treatment of the error propogation gives a resolution width of the form

$$s^2(t)=4(at+bt^2)$$

where a is a configuration dependent constant which is associated with the width of the coordinate measurement,

and b is a configuration dependent constant associated with the finite target length.

Table A3-1 gives the values for the constants a and b for the different experimental configurations used in collecting data.

This naive treatment is a valuable tool for understanding which effects are important in the various t

TABLE A3-1

FIRST ORDER RESOLUTION COEFFICIENTS

E.	a	b
20	19.7×10^{-4}	30.3×10^{-4}
40	10.7×10^{-4}	7.8×10^{-4}
65	7.29×10^{-4}	6.44×10^{-4}
100	5.86×10^{-4}	2.72×10^{-4}
150	5.86×10^{-4}	1.21×10^{-4}
200	6.88×10^{-4}	0.61×10^{-4}

regions. In the low t region the resolution is dominated by the errors in the coordinate measurement; while at high t it is dominated by the target length. In the forward direction, where the resolution affects the extrapolation to zero degrees, the naive treatment fails to give an adequate description.

To get a better representation of the resolution function the individual resolution functions were combined. In performing this combination it proved useful to separate the problem into two parts: finding the distribution of the combined coordinate resolution and finding that of the E and L variables.

The probability distribution of the ratio E^2/L^2 can be represented by the following integral over there individual distributions:

$$P(\eta)d\eta = \iint P(E)dE\ P(L)dL\ \delta(\eta - E^2/L^2)d\eta$$

where η is a particular value of the ratio E^2/L^2.

$P(E)dE$ is the distribution function for E,

and $P(L)dL$ is the distribution function for L.

The distribution in L is due to the finite target length. Since the beam was only attenuated about 5% in passing through the target, it is a fairly good approximation to consider the distribution to be uniform from the targets far end to its near end. The distribution in E is due to the energy spread in the beam. Since this spread was less than 2% and neither the particle yield of the beam nor the interaction cross section being measured vary too rapidly with the beam energy, this distribution can be considered as uniform over the energy acceptance of the beam.

The coordinate distributions are of two kinds: the hodoscope measurements of the beam particle and the detector measurements of the meson position. The hodoscope resolution is dominated by the finite widths of the elements, is nongaussian and depends on the experiment configuration. The distribution of the meson position measurement in the detector is roughly gaussian and results in errors of the same order of magnitude as the hodoscope errors. When these two measurements are combined the resultant distribution for their difference is approximated reasonably well by a gaussian. With this in mind, two difference variables may be introduced to replace the four coordinate measurements. These difference measurements are

defined as follows:

$$x = x_\pi - x_m$$

$$y = y_\pi - y_m$$

Using these variables and the assumption that they are gaussianly distributed, the combined coordinate distribution can be written as

$$P(\xi,\xi')d\xi = \int \frac{e^{-\frac{(x-x')^2}{2\sigma^2}} dx \; e^{-\frac{(y-y')^2}{2\sigma^2}} dy}{2\pi\sigma^2} \times \frac{\delta(x'^2+y'^2-\xi')}{\pi} dx'dy' \; \delta(\xi-x^2-y^2)\, d\xi$$

where ξ is the combined coordinate variable.

P is the probability of measuring a combined coordinate value of ξ given the actual value was ξ',

and σ is the width of the gaussian approximating the distribution of the difference measurements.

Evaluating this integral yields:

$$P(\xi,\xi')d\xi = \frac{e^{-\frac{(\xi-\xi')}{2\sigma^2}}}{2\sigma^2} I_0\left(\frac{\sqrt{\xi\xi'}}{\sigma^2}\right)d\xi$$

where I_0 is the zero order modified Pessel function.

The value of t is just the product of the combined coordinate variable ξ and the energy length ratio η. In terms of their distribution functions the t distribution function is just

$$P(t,t') = P(\xi,\xi')d\xi\, P(\eta)d\eta\, \delta(t-\xi\eta)dt\,\delta(\xi'-t'/\eta)d\xi'$$

where $P(t,t')dt$ is the probability of measuring a value of t in the interval (t,t+dt) if its actual value was t'.

Which reduces to

$$P(t,t') = P\,(t/\eta\,.t'/\eta)/\eta\; P(\eta)d\eta\,.$$

This function is very nongaussian for small values of t′ but begins to look reasonably gaussian for high t′ as shown in figure A3-1. The width of the resolution function agrees quite well with the width calculated in the first order treatment (figure A3-2).

This resolution function was used in fitting empirical functions to the measured data. Given a function describing the differential cross section, the cross section expected in a finite width t bin, where t is measured with an apparatus having a known t resolution, is simply

$$M_i = \int_{t_i}^{t_i+\Delta t_i} \int_0^{\infty} P(t,t')\,dt\,T(t')\,dt'$$

where M_i is the expected cross section in the i^{th} bin,

t_i is the lower limit of the t bin,

Δt_i is its width,

P is the t resolution function,

and T is the function describing the differential cross section.

The fitting was accomplished by minimizing the chisquare defined as

$$\chi^2 = \sum_{bins} (M_i - D_i)^2 / \sigma_i$$

where D_i is the measured data in the i^{th} bin

and σ_i is the statistical error associated with the measurement.

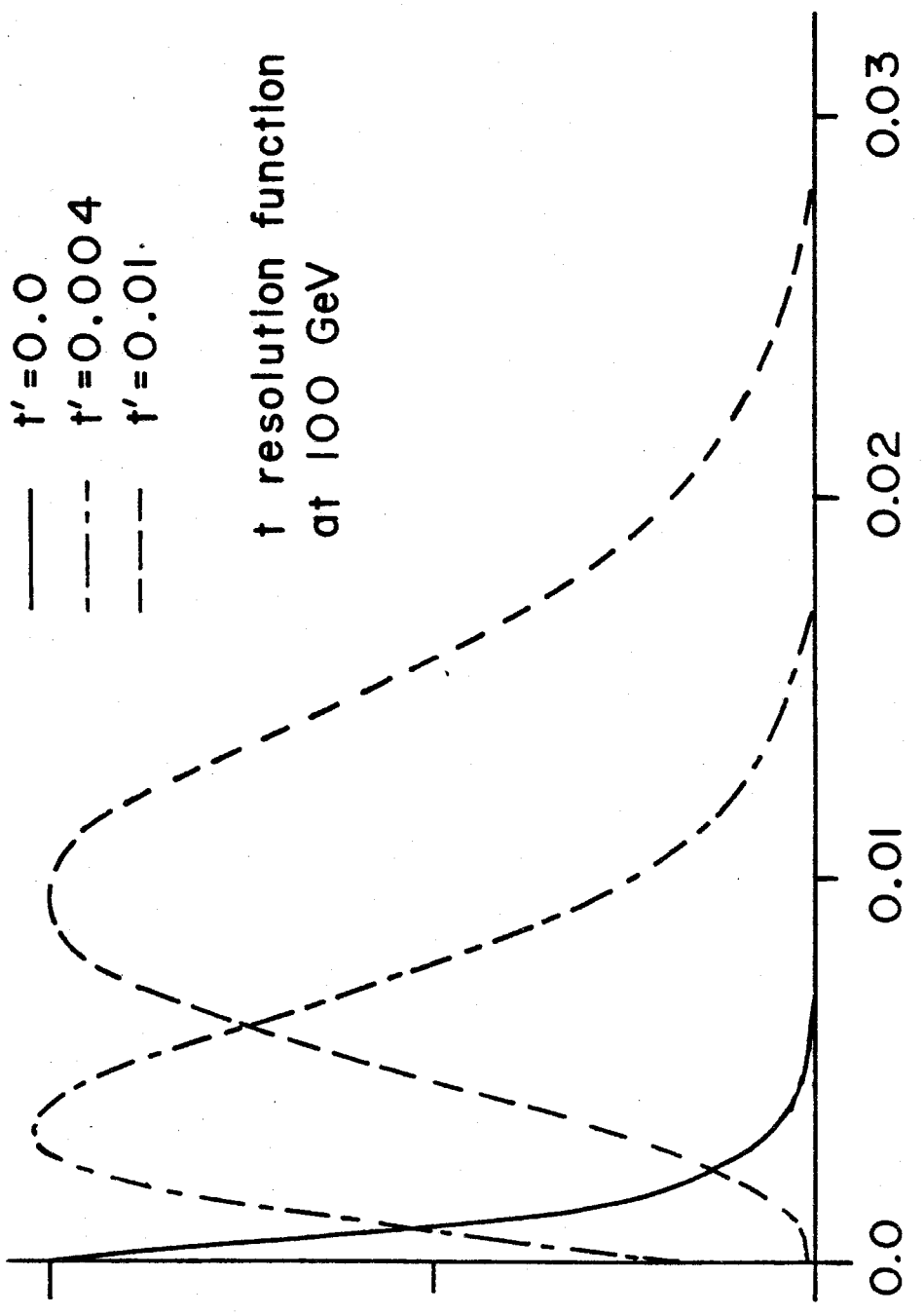
t' = 0.0
t' = 0.004
t' = 0.01
t resolution function
at 100 GeV
P(t,t') unnormalized
0.0
0.01
0.02
0.03
-t (GeV²) ⟶

figure A3-1

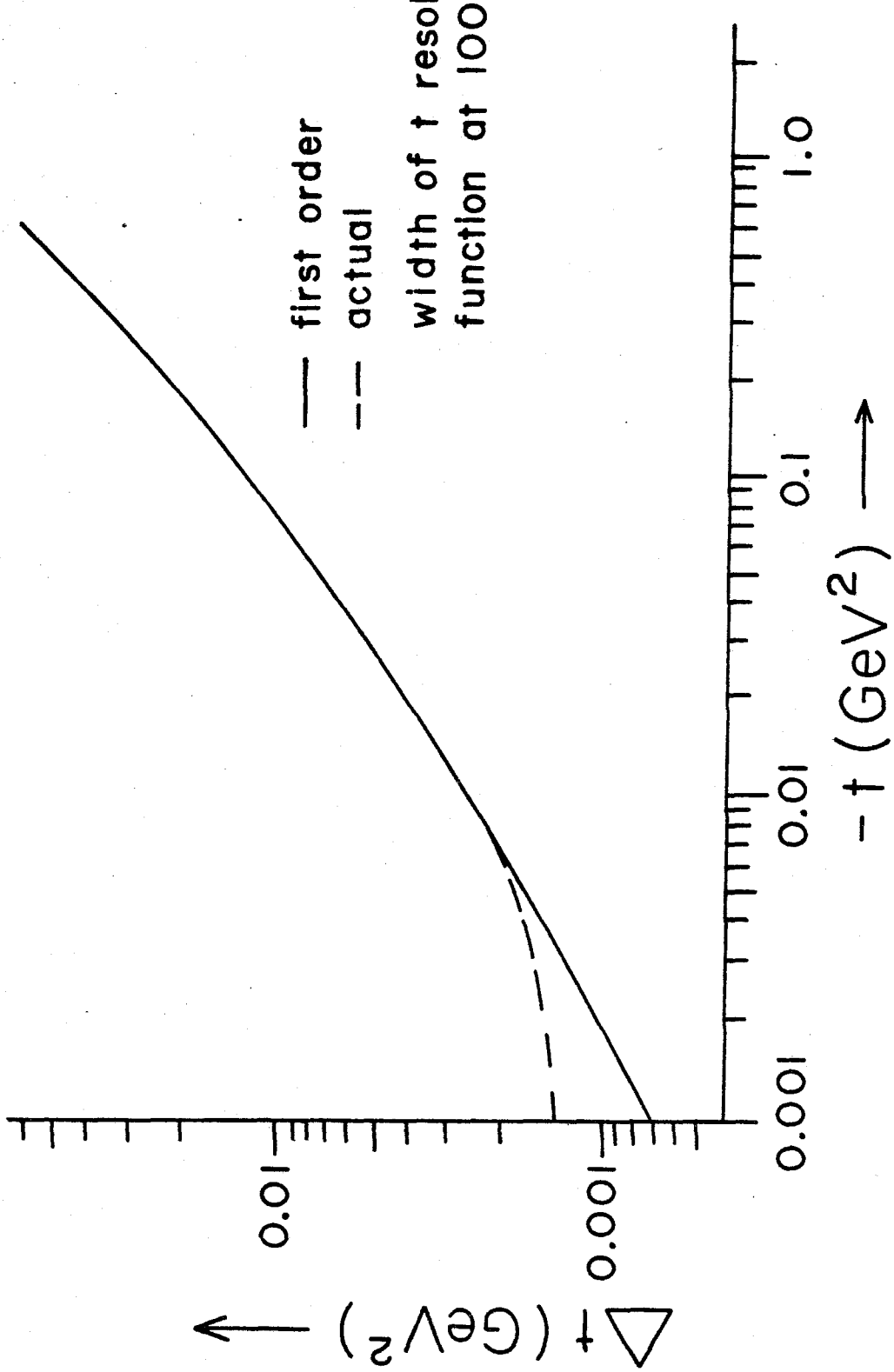
width of t resolution
function at 100 GeV
first order
actual
$\Delta t\ (GeV^2) \longrightarrow$
0.01
0.001
0.0001
0.01
0.1
1.0
$-t\ (GeV^2) \longrightarrow$

figure A3-2

REFERENCES

1-1 A. V. Barnes et al., Phys. Rev. Lett. 37.76(1976); O. I. Dahl et al., Phys. Rev. Lett. 37,80(1976)

1-2 M. Gell-Mann, Phys. Lett. 8,214(1964)

1-3 G. Zweig, CERN Preprints TH401,412(1964)(unpublished)

1-4 H. D. Politzer, Physics Reports 14C(1974); D. Gross and F. Wilczek, Phys. Rev. D8,3633(1973); Phys. Rev. D9,980(1974)

1-5 P. D. B. Collins, "An Introduction to Regge Theory and High Energy Physics" (Cambridge University Press, 1977)

1-6 V. D. Barger and D. B. Cline, "Phenomenological Theories of High Energy Scattering" (Benjamin, New York, 1969)

2-1 R. A. Johnson, thesis, Lawrence Berkeley Laboratory Report LBL-4610(1975)(unpublished)

2-2 P. L. Ford and W. R. Nelson, "The EGS Code System: .." Stanford Linear Accelerator Center report no. SLAC-210 (1978)

2-3 Crannell et al., Phys. Rev. 184,426(1969)

2-4 M. Holder et al., Phys. Lett. 40B,141(1972)

2-5 E. B. Hughs et al., IEEE Transactions on Nuclear Science NS-19,No 3,126(1972)

2-6 R. L. Anderson et al., SLAC-PUB-2039(1977)

2-7 M. A. Wahlig and Mannelli, Phys. Rev. 168.1515(1969);

2-8 R. L. Walker, "Attenuation in long....", CEX note (unpublished)

4-1 Fermi, "Nuclear Physics" (University of Chicago Press, Chicago, 1954)

4-2 R. A. Johnson (private communication)

4-3 R. A. Johnson (private communication)

4-4 R. L. Walker. "The CLEAN Cut", CEX Note (unpublished)

4-5 R. A. Johnson, (private communication)

6-1 Particle Data Group, Phys. Lett. 75B.(1978)

6-2 D. Ebert and M. K. Volkov, JINR Preprint E2-12255(1979); Dass, Phys. Rev. D7,1458(1973)

7-1 W. D. Apel et al., Nucl. Phys. B154.189(1979)

7-2 I. Mannelli et al., Phys. Rev. Lett. 14,408(1965); A. V. Stirling et al., Phys. Rev. Lett. 14,763(1965); P. Sonderegger et al., Phys. Lett. 20,75(1965); M. A. Wahlig and Mannelli, Phys. Rev. 168,1515(1968); V. N. Bolotov et al., Phys. Lett. 38B,120(1972); Nucl. Phys. B37,365(1974)

7-3 P. Bonamy et al., Nucl. Phys. B52,392(1973); D. Hill et al., Phys. Rev. Lett. 30.239(1973)

7-4 V. Barger and R. J. N. Phillips,

7-5 R. R. Desai and P. R. Stevens, Caltech Preprint CALT-68-457(1974)

7-6 T. R. Engelmann and R. E. Hendrick, Phys. Rev. D16.2891(1977)

7-7 S. P. Denisov et al., Nucl Phys. B65,1(1978)

7-8 A. S. Carrol et al., Phys. Rev. Lett. 33,928(1978); Phys. Lett. 61B,303(1976)